The Journal of Chemical Physics

RESEARCH ARTICLE | OCTOBER 29 2026

Recent developments in TURBOMOLE

Special Collection: Electronic Structure Software 2.0

Yannick J. Franzke ; Manas Sharma ; Priyanshi Bhasin ; Florian Bruder ; Uwe Huniar ; Poramas Komonvasee ; Marjan Krstić ; Arman Nejad ; Amber Pausch ; Kesha Sorathia ; Niklas Sülzner ; Ömer Faruk Can Tiska ; Andrew Zhu ; Roman Zielke ; Christof Hättig ; Christof Holzer ; Marek Sierka ; David P. Tew ; Florian Weigend

Check for updates

J. Chem. Phys. 165, 162503 (2026)
https://doi.org/10.1063/5.0351594

View Online
Export Citation

Articles You May Be Interested In

cclib 2.0: An updated architecture for interoperable computational chemistry

J. Chem. Phys. (July 2024)

Interoperable workflows by exchanging grid-based data between quantum-chemical program packages

J. Chem. Phys. (April 2024)

Working with benchmark datasets in the Cuby framework

J. Chem. Phys. (May 2024)

12 November 2026 10:29:21

AIP Publishing

The Journal of Chemical Physics

Special Topics Open for Submissions

Learn More

AIP Publishing

The Journal of Chemical Physics SOFTWARE pubs.aip.org/aip/jcp

Recent developments in TURBOMOLE

Cite as: J. Chem. Phys. 165, 162503 (2026); doi: 10.1063/5.0351594
Submitted: 8 July 2026 • Accepted: 25 September 2026 •
Published Online: 29 October 2026

View Online Export Citation CrossMark

Yannick J. Franzke,[1] Manas Sharma,[2,3] Priyanshi Bhasin,[4] Florian Bruder,[5] Uwe Huniar,[6] Poramas Komonvasee,[7] Marjan Krstić,[8] Arman Nejad,[7] Amber Pausch,[9] Kesha Sorathia,[7] Niklas Sülzner,[10] Ömer Faruk Can Tiska,[10] Andrew Zhu,[7] Roman Zielke,[5] Christof Hättig,[10,a] Christof Holzer,[5,a] Marek Sierka,[2,a] David P. Tew,[7,a] and Florian Weigend[5,a]

AFFILIATIONS

[1]Institute of Nanotechnology, Karlsruhe Institute of Technology (KIT), Kaiserstraße 12, 76131 Karlsruhe, Germany
[2]Otto-Schott-Institut für Materialforschung, Friedrich-Schiller-Universität Jena, Löbdergraben 32, 07743 Jena, Germany
[3]Department of Chemical Engineering, Indian Institute of Science, Bengaluru, Karnataka 560012, India
[4]Department of Physics, Indian Institute of Science, Bengaluru, Karnataka 560012, India
[5]Institute of Quantum Materials and Technologies, Karlsruhe Institute of Technology (KIT), Kaiserstraße 12, 76131 Karlsruhe, Germany
[6]Dassault Systèmes Deutschland GmbH, Am Kabellager 11-13, 51063 Cologne, Germany
[7]Physical and Theoretical Chemistry Laboratory, University of Oxford, South Parks Road, Oxford OX1 3QZ, United Kingdom
[8]Institute of Theoretical Solid State Physics, Karlsruhe Institute of Technology (KIT), Kaiserstraße 12, 76131 Karlsruhe, Germany
[9]Organisch-Chemisches Institut and Center for Multiscale Theory and Computation, University of Münster, Corrensstraße 36, 48149 Münster, Germany
[10]Lehrstuhl für Theoretische Chemie, Ruhr-Universität Bochum, 44780 Bochum, Germany

Note: This paper is part of the Special Topic on Electronic Structure Software 2.0.

[a]**Authors to whom correspondence should be addressed:** christof.haettig@ruhr-uni-bochum.de; holzer@kit.edu; marek.sierka@uni-jena.de; david.tew@chem.ox.ac.uk; and florian.weigend@kit.edu

ABSTRACT

TURBOMOLE is a general-purpose quantum-chemical and materials science program suite for large-scale and high-throughput simulations of molecules and periodic systems of arbitrary dimensionality. The primary focus is on robust and highly efficient methods from first principles. Applications range from the interpretation or even prediction of various spectroscopic results to the elucidation of catalytic or reaction mechanisms. In this review, we summarize the latest developments between 2020 and 2026, consisting of substantial advances in density functional theory and coupled-cluster methods of ground and excited states, relativistic approaches for magnetic properties, and embedding or multiscale frameworks. In addition, the introduction of a new complete active space and configuration interaction module extends the capabilities of the program suite to multireference systems with strong static correlation. Finally, the user-friendliness was greatly improved with TURBOMOLE version 8.0 (2025) by new input formats and default settings making simulations easily possible for expert and non-expert users with a diverse chemical, physical, materials science, or biochemical education and training.

© 2026 Author(s). All article content, except where otherwise noted, is licensed under a Creative Commons Attribution (CC BY) license (https://creativecommons.org/licenses/by/4.0/). https://doi.org/10.1063/5.0351594

12 November 2026 10:29:21

I. INTRODUCTION

TURBOMOLE is a modular program suite consisting of highly efficient methods in electronic structure theory with Gaussian-type basis functions. Initially started in the late 1980s by the group of Ahlrichs,[1] the program suite has successfully developed into a collaborative, multinational software development project to study molecules, clusters, periodic systems, and complex multiscale frameworks with widely available cost-efficient computer hardware.[2–5]

A general overview of the program suite was given in the previous special issue[6] in 2020, highlighting several key methods,[3] such as density functional theory (DFT) approaches up to the level of meta-generalized gradient approximations (meta-GGAs) and local hybrid functionals (LHFs) for ground and excited-state calculations;[7–10] post-Kohn–Sham theories, such as the random phase approximation,[11,12] (RPA) or the Bethe–Salpeter equation (BSE) within the Green's function *GW* approximation;[13–15] low-scaling wavefunction-based and coupled-cluster (CC) formalisms,[16,17] such as CC2 or ADC(2), as well as efficient pair natural orbital (PNO) approaches for coupled-cluster singles and doubles (CCSD) and CCSD with perturbative triples [CCSD(T)].[18–21] Thanks to the support of relativistic pseudopotentials and all-electron Hamiltonians, reliable and accurate simulations are performed throughout the periodic table of elements.[22–25] Solvent and environmental effects can be treated with the conductor-like screening model (COSMO) in its pure dielectric version or the more advanced approach for real solvents (DCOSMO-RS), which is based on the COSMO-RS theory.[26–29] A key feature of the program suite is the rigorous application of integral-direct methods and the density fitting or resolution of the identity (RI) approximation,[30–34] which is further combined with Laplace transform, fast multipole-accelerated (MARI-J), or PNO approaches for extended systems. The use of Gaussian basis functions and the combination of RI and continuous fast multipole methods[35–37] allows us to treat molecules and periodic systems on an equal footing as reviewed very recently.[5] Overall, TURBOMOLE is a flexible and robust tool for chemistry, physics, materials science, and related fields.

In this review, we focus on recent developments. Between 2020 and 2026, the general capabilities for spectroscopy were greatly enhanced in terms of properties that can be calculated, computational methods, the support of relativistic effects, and the introduction of embedding or multiscale frameworks to study complex materials. The program now covers a wide range of functionalities as illustrated in Table I. Accordingly, TURBOMOLE supports the calculation of almost all spectroscopic properties such as Raman or infrared (IR) spectra, fluorescence, and absorption spectra in the UV/vis or X-ray range, as well as magnetic resonance spectra of closed- and open-shell systems. Here, nuclear magnetic resonance (NMR) and electron paramagnetic resonance (EPR) spectra can be simulated. Mössbauer parameters, such as the isomer shift or the electric field gradient (EFG), and the nuclear quadrupole interaction can be further evaluated to complement the experimental findings. Almost all modules are now fully parallelized with OpenMP throughout the whole calculation. The message passing interface (MPI) is further widely available for correlated wavefunction-based approaches, such as CC2 or PNO-CCSD, while graphical processing units (GPUs) are supported for Kohn–Sham DFT methods. A detailed list of all supported parallelizations for each module is available in Ref. 4.

II. NEW INPUT AND DEFAULTS

Initially, the program suite was designed for expert users conducting in-depth studies of individual molecular systems. To support this, TURBOMOLE has always provided a highly flexible and comprehensive toolbox, complemented over time by a growing collection of scripts and utilities that simplify input generation and workflow management.[38–41] Throughout more than three decades of active development, maintaining backward compatibility has been a key design principle, resulting in a stable interface and long-lasting default settings.

With the increasing importance of automated high-throughput studies, machine-learning datasets, and materials and drug discovery workflows, version 8.0 extends this philosophy by offering significantly improved support for automated input generation and more suitable default settings for unsupervised calculations. The modular design, which allows tools to be combined in virtually any order, integrates naturally into modern script-based workflows while preserving the stability and flexibility that have long been hallmarks of the program suite.

A. Simple input

Since the current main release with version 8.0.1 (2026), the simplest input requires only coordinates and a basis set to run Hartree–Fock (HF) or MP2/CC2 calculations. A minimal DFT input for a charge-neutral system at the PBE/def2-TZVP level[42,43] accordingly only requires to define the functional, the basis set, and the molecular structure. Therefore, the complete input file simply reads

```
$coord file=coord
$atoms
   basis = def2-TZVP
$dft
   functional pbe
$end
```

In contrast to the interactive input generators define and TmoleX, where additional options must be specified explicitly, this type of input triggers a series of automatic processes as follows:

- Symmetry is detected and activated. Note that two-component approaches do not support symmetry.
- Adding effective core potentials (ECPs) in case the basis set and elements require those.
- Start orbitals are generated via superposition of atomic densities (SAD), using partial charges as determined from Grimme's electronegativity equilibration (EEQ) model for xTB.[44] For charged systems, the charge has to be added in the input file explicitly. Electronic configurations of the elements are tabulated for H–Lr in V8.0 and for H–Og in V8.1, with the application of partial charges being straightforward. In two-component Kramers-unrestricted runs, the spin configuration is assigned accordingly to set up the spin magnetization vector.

12 November 2026 10:29:21

© Author(s) 2026

TABLE I. Available spectroscopic properties in non-relativistic and relativistic frameworks with various levels of theory. The relativistic approaches are either available in a one-component (1c) formalism or the full relativistic two-component (2c) approach with a variational and self-consistent treatment of spin–orbit coupling. Two-component MP2, CC2, and RPA treatments are not possible for the Mössbauer parameters and the EPR hyperfine coupling, but the impact of spin–orbit coupling has to be calculated at the underlying HF or KS method. COSMO is available throughout to account for counterions or solvent effects. Optical properties also widely support embedding schemes for a more sophisticated treatment. Parentheses indicate that the property can only be calculated with numerical gradients or are restricted to certain systems.

Property	Non-relativistic	1c relativistic	2c relativistic	Level of theory
UV/Vis fluorescence & absorption	✓	✓	✓	DFT, *GW*-BSE, HF, CC2, CC3, ADC(2)
X-ray absorption	✓	✓	✓	DFT, *GW*-BSE, HF, CC2, CC3, ADC(2)
High harmonic generation	✓	✓	✗	DFT, HF
Circular dichroism	✓	✓	✓	DFT, *GW*-BSE, HF, CC2, CC3, ADC(2)
Vibrational circular dichroism	✓	✓	✗	DFT, HF
Infrared and Raman	✓	✓	(✓)	DFT, (RPA), HF, MP2, CC2
NMR shifts	✓	✓	✓	DFT, HF, MP2
NMR coupling	✓	✓	✓	DFT, *GW*-BSE, HF
EPR g-tensor	✓	✓	✓	DFT, HF
EPR hyperfine coupling	✓	✓	✓	DFT, RPA, HF, MP2, CC2
Zero-field splitting	✓	✓	(✓)	DFT, HF (only axial symmetry for 2c)
EFG and NQI	✓	✓	✓	DFT, RPA, HF, MP2, CC2
Mössbauer isomer shift	✓	✓	✓	DFT, RPA, HF, MP2, CC2

- RI approximation (and multipole-accelerated RI) is automatically added when modules using RI are called; suitable auxiliary basis sets are taken from the internal basis set library.
- During geometry optimizations, internal redundant coordinates are generated and used.

B. New defaults in version 8.0 and beyond

Some of the old defaults are no longer appropriate—such as the maximum of 30 self-consistent field (SCF) iterations. This was the main reason why only 307 of 329 of the M06-2X[45] cases converged with TURBOMOLE in the benchmark set[46] that was used to compare Accelerated DFT,[46] PySCF,[47] and TURBOMOLE.[48]

Therefore, version 8.0 included major updates for several default settings. Besides the maximum number of SCF iterations and more strict convergence criteria, which now include a density convergence check for HF by default, the def basis sets[49] were replaced by the def2 basis sets[43] when using the command-line input module define or the graphical user interface TmoleX. COSMO now uses Gaussian charges to ensure continuous potential energy surfaces and avoid artificial imaginary frequencies.[50] Likewise, the default functional was changed to Perdew–Burke–Ernzerhof (PBE)[42] with medium-sized grids and weight derivatives enabled by default. This was motivated by the observation that the computation time for the DFT exchange–correlation potential is usually not the time-determining part of a calculation and that the m-grids,[51] initially introduced to speed up calculations, are not sufficiently accurate for many spectroscopy tasks, such as NMR or EPR properties. Starting with version 8.0.1 (2026), a superposition of atomic densities (SAD) is the default initial guess and the evaluation of integrals for this guess makes use of the same approximations as the following SCF procedure to ensure consistency and efficiency. The SAD with natural orbitals to construct the full density directly and avoid the diagonalization of a Fock matrix in the guess (SADNO) is also available.[52] A full list of default changes is given in a separate section of the manual.[53,54] This simplification and increase in robustness will continue in future release, such as version 8.1 (December 2026), where the canonical orthogonalization becomes fully available across all SCF paths and the condition number of the overlap matrix will be calculated right in the beginning to advice the user to turn on the canonical orthogonalization if necessary. We envision that this will make the program suite more accessible to a broad user base.

The cumulative impact of these changes can be illustrated using the 329 test cases discussed above. In earlier versions, convergence problems could often be avoided by increasing the maximum number of SCF iterations and/or by employing second-order SCF solvers, such as the augmented Roothaan–Hall (ARH) method (`$arh` keyword) from the outset. With the new input format and default settings, however, 327 of the 329 calculations converge without difficulty using only the conventional direct inversion in the iterative subspace (DIIS) procedure, requiring fewer than 16 iterations on average.

It is worth noting that, for the remaining two cases, the published total energies[55] do not correspond to the ground-state minima. Stability analyses[56] reveal pronounced triplet instabilities[57] in both systems. The improvement resulting from the new superposition-of-atomic-density initial guess is particularly evident for FeBF4 ($C_{22}FeH_{18}N_{10}$), where the number of SCF iterations decreases from 147 to 46. For this system, the closed-shell singlet energy obtained with TURBOMOLE is −79.5 kcal/mol lower than the reported value, irrespective of the choice of initial orbitals.

The new input format combined with the new defaults and settings are a great help in making it easy to perform automated calculations in many systems, but it is advisable to stick to the good old practice of healthy skepticism and, at the very least in the case of an unusually high number of SCF iterations, to carry out an

12 November 2026 10:29:21

© Author(s) 2026

instability check to avoid ending up with an incorrect electronic state.

C. Exploitation of symmetry for spectroscopy

As evident from the automatic detection of symmetry, TURBOMOLE supports Abelian and non-Abelian molecular point group symmetry for SCF and post-SCF runs, including the initial guess, integral evaluation, and DFT grid construction. The irreducible representations can be further exploited to study selected excitations and their properties. The most drastic speed-up with symmetry is observed for geometry gradients and Hessians, as this allows easily optimize molecular structures by only considering non-redundant nuclear centers.[1–3,58–62]

For nuclear-dependent properties, such as NMR coupling constants, point-group symmetry is supported for non-dihedral groups to accelerate the calculations and can be additionally combined with nuclear selection schemes.[63] The same holds for the related EPR hyperfine coupling tensor. Calculations of the NMR shielding tensors and the EPR g-tensor support point groups without reducible E representations.[60,64] This scheme is also made available for the zero-field splittings (ZFSs) in the developers' version and will be made publicly available in V8.2.

Beyond the modules for non-relativistic and scalar-relativistic energies and (response) properties, support of symmetry is not available at present. That is, relativistic two-component calculations do not support point symmetry at all. The same holds for the new multireference module in one-component and two-component calculations. The `riper` module for molecular and periodic calculations of arbitrary dimensionality does not support point or space groups.[5] This means that also real-time spectroscopic properties currently have to be computed in C_1 symmetry.

D. Online manual

Complementing the printable reference manual,[53] a fully searchable online manual is now available at https://manual.turbomole.org.[54] Its content is generated automatically from the same LATEX sources that are shipped with each release, so that the online version stays consistent with the program and can be regenerated for every new release, with mathematical expressions rendered faithfully in the browser. A two-tier search combines an alphabetical index of all input keywords and commands with a full-text search across the entire manual.

Beyond static documentation, the site provides interactive resources that lower the barrier for new and non-expert users. A growing collection of curated, ready-to-run input examples covers typical tasks, such as DFT and wavefunction-based energies, geometry optimizations, vibrational frequencies, second-order perturbation theory and coupled-cluster calculations, excited states from time-dependent density functional theory (TDDFT) and ADC(2), *GW* quasiparticle energies, NMR shieldings, COSMO solvation, and calculations on periodic systems. Each example was validated by running it with TURBOMOLE and can be downloaded directly. In addition, an interactive input generator assembles a complete input file from a few choices, such as the type of calculation, method, density functional, basis set, integral approximation, dispersion correction, and solvation, while a companion structure tool converts common geometry formats into TURBOMOLE geometry input and detects the molecular point group. Together with the simplified input format and updated defaults described above, these tools make TURBOMOLE more accessible to a broad and diverse user base.

E. A new geometry optimizer

For most production work, the limiting cost is not a single energy evaluation but the geometry optimization wrapped around it, where energy and gradient are recomputed at every step until the forces fall below threshold. A run's cost, therefore, comes down to the number of these steps. The forthcoming version 8.1 introduces a new optimizer, used by default, that aims to reduce that number while requiring no user choices about coordinate systems, starting Hessians or step damping.

The method stays in Cartesian coordinates and starts from an approximate Hessian of the Lindh type,[65] whose force constants follow from interatomic connectivity rather than from a second-derivative calculation. That model is improved as the optimization runs, and a quasi-Newton step with adaptive trust radius is taken from it on each cycle.[66] There is no line search and no exact Hessian, so a cycle costs one energy and one gradient and nothing more, whatever produces them. The same optimizer handles Hartree–Fock, density-functional, correlated wavefunction, and tight-binding methods, for both molecules and periodic systems, and it is reached through the usual `jobex` driver.

Lindh's original parameters cover the first three rows of the periodic table, and they are used unchanged whenever both atoms of a pair belong to these rows. For a pair involving a heavier element, the reference distance is instead assembled from the single-bond covalent radii of Pyykkö and Atsumi,[67] which are tabulated for the elements 1–118, and is scaled by a factor depending on the covalent coordination numbers[68] of the two atoms, which accounts for the lengthening of bonds on passing from molecular to metallic coordination. The f-block elements are represented by lanthanum and actinium. The model Hessian is, thus, available throughout the periodic table and requires no element-specific input.

To gauge it, we used a set of 1752 molecules of 4–110 atoms, drawn from the Baker test set,[69] a wide selection of GMTKN55 subsets,[70] the 130 transition-metal complexes of the tmQM database,[71] a curated set of 100 organic molecules, and the larger drug-like molecules of Birkholz and Schlegel.[72] Among them are 215 charged species and 114 open-shell doublets. Each molecule is relaxed on the GFN2-xTB surface[73] from a deliberately distorted starting geometry, the same for every optimizer. Every optimizer is held to one externally applied criterion, a maximum Cartesian gradient component under 10^{-4} a.u. with an energy change under 10^{-6} a.u., rather than its own native test, and its cost is the number of GFN2-xTB energy and gradient evaluations it uses to reach that point, counted the same way throughout.

Table II sets the new optimizer against three open-source codes: geomeTRIC,[74] which builds translation-rotation internal coordinates, the native optimizer of the xtb program,[75] which works in approximate normal coordinates, and the Cartesian optimizers of the Atomic Simulation Environment (ASE).[41] The new optimizer converged all 1752 structures, the 130 transition-metal complexes among them, at the lowest cost in the comparison, a median of 19 evaluations. geomeTRIC and the xtb optimizer each failed only a handful and ran to a median of 29 and 36 evaluations, respectively;

12 November 2026 10:29:21

© Author(s) 2026

TABLE II. Energy minimization of 1752 molecules from distorted starting geometries on the GFN2-xTB surface to a common criterion (maximum gradient component below 10^{-4} a.u. and energy change below 10^{-6} a.u.). The median and mean columns give the number of energy-and-gradient evaluations over the converged structures. The ASE rows are the strongest quasi-Newton variant (BFGSLineSearch), the GoodOldQuasiNewton scheme, the limited-memory L-BFGS, and the first-order FIRE method.

Optimizer	Converged (%)	Median	Mean
New optimizer	100.0	19	26.8
geomeTRIC (TRIC)	99.8	29	37.4
xtb (ANC)	99.7	36	47.5
ASE BFGSLineSearch	98.7	66	86.7
ASE GoodOldQuasiNewton	98.1	50	64.9
ASE L-BFGS	96.6	68	83.6
ASE FIRE	73.0	131	144.5

the strongest Cartesian quasi-Newton scheme in ASE reached 98.7% at a median of 66, whereas the first-order FIRE method reached 73%. The separation grows in the mean, where the hard cases raise the other codes to 37 to 145 evaluations against 26.8 for the new optimizer. Internal coordinates are usually expected to shorten an optimization, yet here the Cartesian scheme needs fewer evaluations than the internal-coordinate code, which suggests that their reputed advantage need not hold once the model Hessian and step control are well chosen. The complete set of starting geometries, converged structures, optimization paths, and reference minima has been deposited.[76]

First-order saddle points are found with the same machinery. For a transition state, the model Hessian supplies one ascent direction to climb while the remaining coordinates relax,[77,78] again at one gradient per cycle and without an exact Hessian. We checked this on RGD1-TSopt-GFN2,[79] a benchmark of 1500 GFN2-xTB transition states taken from the RGD1 reaction database,[80] a collection of elementary reactions of organic molecules built from C, H, N, and O with at most ten non-hydrogen atoms, each given three distorted starting geometries of increasing amplitude. Starting from the undistorted reference geometry, the correct saddle returns in every case. Table III shows how this fidelity falls under distortion: the reference-saddle column, the share of runs that come back to the specific reference saddle, drops from 78% to 51% and 32% across the three tiers. The any-saddle column adds the runs that settle at a different but genuine first-order saddle, and the two columns diverge as the distortion grows and more valid saddles come within reach. A single exact Hessian, evaluated once at the final structure, settles the index, and none is needed during the search itself.

TABLE III. Transition-state search on RGD1-TSopt-GFN2 (1500 GFN2-xTB first-order saddles), each start distorted from the reference by the listed reaction-mode RMSD plus a fixed 0.12 Å along the other modes. The columns give the fraction of runs reaching the reference saddle and any genuine first-order saddle.

Tier	RMSD (Å)	Reference saddle (%)	Any valid saddle (%)
Easy	0.06	77.6	84.2
Medium	0.11	50.5	67.1
Hard	0.15	32.1	58.7

The reactions collected in that benchmark are organic ones, in which the reaction coordinate is a bond between light main-group atoms being formed or broken, and this is the situation a connectivity-based model Hessian describes best. Reactions at a metal center are more demanding, chiefly in the initial choice of the ascent direction: dative metal-ligand bonds are soft, and the low-curvature part of the model spectrum is crowded with ligand rotations and skeletal deformations of comparable stiffness, so the softest mode need not be the one that leads to the saddle. For metal-catalyzed steps, we, therefore, expect the recovery rates of Table III to be lower, and a starting structure close to the saddle to matter more. The ascent direction may then be taken from computed rather than modeled curvature: an analytic Hessian may be supplied, in which case the search follows its most negative eigenvector, while an inexpensive semi-empirical Hessian evaluated at the GFN2-xTB level serves the same purpose at a fraction of the cost. Alternatively, the reaction mode may be selected by its index or given as an explicit Cartesian direction. None of this is needed by default; unless one of these options is requested, the search runs on one energy and gradient per cycle as described above.

III. DENSITY FUNCTIONAL THEORY

A. Expansion of local hybrids: Toward general density functionals

Recent developments in DFT within TURBOMOLE are geared toward a broad applicability of new density functional approximations (DFAs) to as many systems as possible. Local hybrid functionals provide an excellent basis for this task, as a local hybrid functional is controlling the amount of Hartree–Fock exchange or exact exchange locally in real space. This yields the exchange–correlation energy expression,[8,81]

$$E^{\mathrm{XC}} = \int \mathrm{d}\mathbf{r}\; a(\mathbf{r}) e_{\mathrm{X}}^{\mathrm{HF}}(\mathbf{r}) + (1 - a(\mathbf{r})) e_{\mathrm{X}}^{\mathrm{DFA}}(\mathbf{r}) + \rho(\mathbf{r}) \varepsilon_{\mathrm{C}}^{\mathrm{DFA}}(\mathbf{r}), \quad (1)$$

where the local mixing function is defined as

$$a(\mathbf{r}) = f(\rho, \nabla\rho, \tau), \qquad 0 \le a(\mathbf{r}) \le 1 \quad (2)$$

with the density ρ, its gradient $\nabla\rho$, and the kinetic-energy density τ. Developments of LHFs have, therefore, been a key part of TURBOMOLE's DFT philosophy in the recent years. Previous types of LHFs having been discussed in earlier reviews[3,4] tend to suffer from rather high parameterization. Therefore, TURBOMOLE has decided to follow a completely new path of density functional design, the generalized fermion functional (GFF).[82] Decades of developing density functionals based on chemical information has shown that processing information from electrons only is not sufficient to yield radically new density functional approximations, which improve the description of properties across the periodic system of elements. The design of GFFs follows the philosophy "Constraints first, fit second": recover the right limits, respect the structure of one- and two-particle systems, and let the local mixing function decide where exact exchange is needed. The key improvement is, therefore, not simply a larger fraction of Hartree–Fock exchange, but its more appropriate distribution: enhanced where self-interaction errors are most severe,

12 November 2026 10:29:21

© Author(s) 2026

reduced where semilocal exchange is sufficient, and smoothly varying across chemically distinct regions. Missing pieces that could not be recovered from electronic systems have been confined by inter-fermionic interactions via multifermion DFT.[83] In a multifermion setting, the density is no longer a single electronic object, but a set of fermionic densities,

$$\rho_{\mathrm{e}}(\mathbf{r}), \rho_{\mathrm{p}}(\mathbf{r}), \rho_{\mu}(\mathbf{r}), \ldots, \tag{3}$$

so that exchange and correlation must remain meaningful for electrons (e), protons (p), muons (μ), or other quantum fermions,

$$E^{\mathrm{XC}} \rightarrow E^{\mathrm{XC}}[\rho_{\mathrm{e}}, \rho_{\mathrm{p}}, \rho_{\mu}, \ldots]. \tag{4}$$

This is where the local-hybrid GFF construction becomes especially powerful: strongly localized fermions can require very different amounts of exact exchange than delocalized electronic densities,[82,83]

$$a(\mathbf{r}) = f_{\alpha}(\rho_{\alpha}, \nabla\rho_{\alpha}, \tau_{\alpha}), \qquad \alpha \in \mathrm{e}, \mathrm{p}, \mu, \ldots. \tag{5}$$

Rather than building a separate empirical functional for every particle type, the newly developed CHYF functional[82] aims for a transferable blueprint: derive the functional form from constraints and then adapt it to the fermionic component through its local density descriptors. For electron–proton systems, this naturally introduces explicit inter-fermion correlation,

$$\int \mathrm{d}\mathbf{r}\ \varepsilon_{\mathrm{C}}^{\mathrm{e-p}}(\rho_{\mathrm{e}}, \rho_{\mathrm{p}}, \nabla\rho_{\mathrm{e}}, \nabla\rho_{\mathrm{p}}, \ldots), \tag{6}$$

turning CHYF from an electronic-structure functional into a general many-fermion design principle. It has been shown that this type of functionals is very successfully applicable to various problems, especially tackling electric and magnetic properties as for example NMR shieldings, UV/Vis spectra, and many more in both theoretical benchmark studies[82] and "real-world" applications.[84–87]

B. Multifermion DFT/RPA/GW: Quantum-mechanical treatment of additional fermions

Recent releases mark a substantial broadening of the program from standard electronic-structure theory toward multifermion, response, and Green's-function *GW* methods. A central step is the introduction of multifermion DFT in TURBOMOLE through the `$mcdft` keyword, which allows an additional fermionic quantum particle, for example a proton, muon, positron, or a fermionic nucleus, such as ^{19}F, to be treated together with the electronic system. This update is more than a technical extension of Kohn–Sham DFT: it creates a common platform on which correlation, binding energies, quasiparticle energies, and light–matter interactions of non-electronic particles can be investigated within the same response-theory infrastructure used for electrons to gain in-depth insight into the correlation. In addition, multifermion DFT is a promising method to describe tunneling reactions, proton transfer reactions in biochemical processes, or proton-coupled electron transfer reactions.[88–90]

The theoretical backbone of these developments is the multifermion post-Kohn–Sham framework.[83] In this formulation, the electronic density ρ_{e} and the density of an additional fermion ρ_{f} enter an adiabatic-connection Hamiltonian of the form

$$\hat{H}_{\alpha}(\rho_{\mathrm{e}}, \rho_{\mathrm{f}}) = \hat{T}_{\mathrm{e}} + \hat{T}_{\mathrm{f}} + \hat{V}_{\mathrm{ne}} + \hat{V}_{\mathrm{nf}} + \hat{V}_{\alpha}(\rho_{\mathrm{e}}, \rho_{\mathrm{f}}) + \alpha\left(\hat{V}_{\mathrm{ee}} + \hat{V}_{\mathrm{ef}} + \hat{V}_{\mathrm{ff}}\right), \tag{7}$$

where n denotes the classical nuclei and α continuously connects the non-interacting multifermion Kohn–Sham reference to the interacting system. $\hat{T}$ and $\hat{V}$ refer to the kinetic and potential energy with the indices for the latter classifying the interaction. This equation is important as it demonstrates that electron–electron, electron–fermion, and fermion–fermion interactions can be switched on in a unified way.

The corresponding multifermion RPA correlation energy can be written in a fluctuation–dissipation form,

$$E_{\mathrm{C}}^{\mathrm{RPA}} = \frac{1}{4\pi}\int_0^1 \mathrm{d}\alpha \int_{-\infty}^{\infty} \mathrm{d}\omega\ \mathrm{Tr}\left[\mathbf{V}(\mathbf{\Pi}_{\alpha}(\mathrm{i}\omega) - \mathbf{\Pi}_0(\mathrm{i}\omega))\right], \tag{8}$$

with $\mathbf{\Pi}_{\alpha}$ denoting the interacting multifermion response function and $\mathbf{\Pi}_0$ denoting the Kohn–Sham response. In practice, this expression leads to a plasmon-type formula,

$$E_{\mathrm{C}}^{\mathrm{RPA}} = \frac{1}{2}\left[\sum_n \Omega_n^{+} - \mathrm{Tr}\left(\mathbf{A}'\right) - \mathrm{Tr}\left(\mathbf{A}''\right)\right], \tag{9}$$

$$E_{\mathrm{C}}^{\mathrm{e-f}} = \frac{1}{2}\sum_n \left(\Omega_n^{+} - \Omega_{n,\mathrm{unc}}^{+}\right), \tag{10}$$

where the first expression gives the total RPA correlation energy, while the second isolates the electron–fermion contribution by subtracting an uncoupled reference. The excitation energies Ω_n^{+} are obtained from the multifermion response eigenvalue problem, schematically

$$\begin{pmatrix} \mathbf{A}' & \mathbf{B}' & \mathbf{C}^{\mathrm{T}} & \mathbf{C}^{\mathrm{T}} \\ -\mathbf{B}' & -\mathbf{A}' & -\mathbf{C}^{\mathrm{T}} & -\mathbf{C}^{\mathrm{T}} \\ \mathbf{C} & \mathbf{C} & \mathbf{A}'' & \mathbf{B}'' \\ -\mathbf{C} & -\mathbf{C} & -\mathbf{B}'' & -\mathbf{A}'' \end{pmatrix} \mathbf{Z}_n = \Omega_n \mathbf{Z}_n. \tag{11}$$

Here, primed blocks denote the electronic sector, double-primed blocks denote the additional fermion sector, and **C** denote the coupling between them. **A** and **B** are the orbital Hessian matrices. **Z** is the solution vector. This matrix equation is arguably the key computational object: it shows how electronic and non-electronic density fluctuations become correlated.

The most recent work extends this direction from electron–proton-type examples to the heavier fermionic nuclei ^{13}C and ^{19}F.[91] This emphasizes that the multifermion RPA expression is not merely formal: it can be evaluated for nuclear densities, compared with second-order perturbation theory, and used to diagnose the role of self-interaction errors. In the diagonal limit, the electron–fermion RPA correlation energy reduces to a second-order form,

$$E_{\mathrm{C}}^{\mathrm{e-f,diag}} = \frac{1}{2}\sum_n \left(\Omega_n^{+} - \Omega_{n,\mathrm{unc}}^{+}\right) \Leftrightarrow E_{\mathrm{C}}^{\mathrm{e-f,MP2}}, \tag{12}$$

which provides an important bridge between multifermion RPA and future double-hybrid or perturbative multifermion density functionals.

12 November 2026 10:29:21

© Author(s) 2026

The parallel development of multifermion GW is equally significant. In the multifermion setting, the correlation self-energy of a quasiparticle state q can be decomposed as

$$\Sigma_q^{\mathrm{C}}(\omega^{\mathrm{F}}) = I_q^{\mathrm{C}}(\omega^{\mathrm{F}}) + R_q^{\mathrm{C}}(\omega^{\mathrm{F}}), \tag{13}$$

where the two terms represent the imaginary-axis integral I and residue contributions R in a contour-deformation treatment. The quasiparticle energy is then obtained from the Kohn–Sham eigenvalue plus exchange and correlation self-energy correction to the Kohn–Sham exchange–correlation potential,

$$\varepsilon_q^{\mathrm{QP}} = \varepsilon_q^{\mathrm{KS}} + Z_q\langle q|\Sigma^{\mathrm{X}} + \Sigma^{\mathrm{C}} - v_{\mathrm{XC}}^{\mathrm{KS}}|q\rangle. \tag{14}$$

For a quantum nucleus, this quasiparticle energy corresponds to the energy associated with removing that nucleus from the quantum-mechanical multifermion system. Our recent work shows that this idea is technically feasible for ^{13}C and ^{19}F,[91] but also that vertex corrections become essential as direct RPA can suffer from large self-interaction errors for compact, highly charged nuclear densities.

C. Current-density-dependent meta-GGAs

A central quantity of modern DFAs is the kinetic-energy density,

$$\tau(\mathbf{r}) = \frac{1}{2}\sum_q f_q|\mathbf{p}\psi_q(\mathbf{r})|^2 = \frac{1}{2}\sum_{\mu\nu} D_{\mu\nu}^{\mathrm{RS}}\{[\nabla\chi_\mu(\mathbf{r})][\nabla\chi_\nu(\mathbf{r})]\}, \tag{15}$$

which is formed with the linear momentum operator $\mathbf{p}$ and the Kohn–Sham orbitals ψ_q with the occupation f_q. In practical implementations, this relates to the real and symmetric density matrix $\mathbf{D}^{\mathrm{RS}}$ of the real basis functions χ_μ and χ_ν. At the meta-GGA level, these variables are applied to identify inhomogeneities and the iso-orbital regions of the electron density based on the von Weizsäcker kinetic-energy density. Here, the inhomogeneity parameter z is defined according to

$$z(\mathbf{r}) = \frac{\tau_{\mathrm{W}}(\mathbf{r})}{\tau(\mathbf{r})} = \frac{|\nabla\rho(\mathbf{r})|^2}{8\rho(\mathbf{r})\tau(\mathbf{r})} \quad \text{with} \quad 0 \le z(\mathbf{r}) \le 1, \tag{16}$$

where a value of $z \approx 1$ denotes iso-orbital regions. Therefore, z is of great importance to cancel the self-interaction error. For electromagnetic properties, τ and related quantities, such as the electron localization function, necessitate an extension to ensure that the inequality above still holds and to ensure gauge invariance.[7,92–94] This requirement can be easily rationalized by the inclusion of the momentum operator in the kinetic-energy density and the introduction of magnetic properties with the principle of minimal coupling. Then, the kinetic-energy density is generalized to[92–94]

$$\tilde{\tau}(\mathbf{r}) = \tau(\mathbf{r}) - \frac{|\mathbf{j}(\mathbf{r})|^2}{2\rho(\mathbf{r})} \tag{17}$$

with the paramagnetic current density,

$$\mathbf{j}_{\mathrm{p}}(\mathbf{r}) = -\frac{\mathrm{i}}{2}\sum_q f_q\left[\psi_q^*(\mathbf{r})\nabla\psi_q(\mathbf{r}) - \psi_q(\mathbf{r})\nabla\psi_q^*(\mathbf{r})\right], \tag{18}$$

for magnetic properties, such as NMR shifts[10,95,96] and couplings,[10] EPR g-tensors,[96] electron–nucleus hyperfine couplings,[97] zero-field splittings,[98] as well as excitation energies[7] and excited state properties.[99] For the given properties, the ground state is unaffected, but an extension of the exchange–correlation kernel due to the current density response from the perturbation is required. This is due to the fact that the current density only arises with an imaginary and antisymmetric density matrix $\mathbf{D}^{\mathrm{IA}}$, which is induced by an antisymmetric or non-symmetric perturbation, i.e.,

$$j_{\mathrm{p},u}(\mathbf{r}) = -\frac{1}{2}\sum_{\mu\nu} D_{\mu\nu,u}^{\mathrm{IA}}[\{\nabla_u\chi_\mu(\mathbf{r})\}\chi_\nu(\mathbf{r}) - \chi_\mu(\mathbf{r})\{\nabla_u\chi_\nu(\mathbf{r})\}] \tag{19}$$

becomes non-zero. The impact or practical importance of the generalization on the actual results strongly depends on the functional and the chemical system. On the one hand, the Minnesota functionals[45] and the SCAN functionals[100] are highly affected by the current density. On the other hand, TPSS[101] or hybrid functionals with a large amount of exact exchange are subject to rather small effects. Here, the exact exchange already incorporates the current density and consequently mitigates the error from not including it for the kinetic-energy density.

For simplicity and consistency, the current-dependent formulation of the kinetic energy density is now the default in non-relativistic and scalar-relativistic calculations. This choice ensures consistency of the time-dependent DFT (TDDFT) and NMR/EPR properties. In practice, this always necessitates an iterative solution of the response equations—already for semilocal or pure meta-GGAs. However, these iterations do not substantially increase the computational costs of the complete workflow, which are usually dominated by the structure optimization.

For calculations beyond perturbative approaches, such as finite magnetic fields[102,103] or real-time TDDFT (RT-TDDFT),[5] the kinetic-energy density needs to be generalized directly at the energy and potential level for the SCF or SCF-like procedure. The same applies for relativistic two-component (2c) spin–orbit approaches, as spin–orbit coupling is a form of magnetic induction.[104] This leads to the framework of current density functional theory (CDFT) and ensures that results in the presence of finite magnetic fields are independent of the position of the molecule in space. CDFT is implemented for the ground-state energies and gradients as well as excitation energies of both finite magnetic field calculations and relativistic *Ansätze*.[105–108] For relativistic effects, the NMR and EPR properties are also available with spin–orbit CDFT.[106] Moreover, periodic CDFT calculations are possible for the SCF part and structure optimizations, including both the atomic positions in the unit cell and lattice vectors.[107,108] Here, the current density is of great importance for Rashba splittings as reviewed recently.[5]

IV. COUPLED-CLUSTER METHODS

TURBOMOLE has supported accurate wavefunction methods for computing the ground state energy of molecular configurations since 2010. The characteristics of the implementation of MP4, CCSD(T), BCCD(T), and their F12 explicitly correlated counterparts[109–111] are low memory and disk requirements, achieved through a hybrid integral-direct and density fitting strategy, and shared-memory parallelization. Using F12 methods, near basis set

12 November 2026 10:29:21

© Author(s) 2026

limit CCSD(T) calculations on systems with 20–30 atoms are routinely possible, enabling quantitative comparison with experiment for thermochemistry, kinetics, and spectroscopy.

TURBOMOLE V7.5 (2020) saw the release of low-scaling variants of MP2, MP3, CCSD(T), and their F12 extensions, where pair-natural orbital theory using localized molecular orbitals, local density fitting, and Laplace transformation was used to exploit the locality of electron correlation.[18–20,112,113] In 2021, the extension to the projected atomic orbital (PAO) domain-based PNO theory was completed,[21,114] resulting in a near-linear scaling implementation with a single parameter, the PNO occupation number threshold, which controls the severity of the PNO approximation. Domain-based local pair natural orbital CCSD(T) [DLPNO-CCSD(T)] and DLPNO-CCSD(T)-F12 are available for both closed- and open-shell systems, using an unrestricted spin formalism, with consistent local approximations in the restricted and unrestricted HF regimes (RHF/UHF).

A. DLPNO-CCSD(T)

The TURBOMOLE code employs a highly efficient orbital-specific-virtual (PAO-OSV-PNO) cascade to determine the PAO and PNO pair domains.[21,114] At each step, the virtual orbital domains are determined using a spin-averaged approximate MP2 density, using thresholds linked to the PNO occupation number threshold. This generates small pair domains without additional loss of accuracy. At the CCSD level, the TURBOMOLE code also employs the multilevel approximation, where short-range higher-order interactions are discarded for pairs with small MP2 pair energies.[115] A "direct" option is available, where the integrals with three and four PNO indices are evaluated at every iteration instead of storing them on disk. This reduces disk requirements by an order of magnitude with a moderate increase in run time.

The default setting is to use the tight PNO threshold of $\mathscr{T} = 1 \times 10^{-7}$. The convergence to the canonical energies is smooth and follows a $E_{\mathscr{T}} = E_\infty + A\mathscr{T}^{1/2}$, and a two-point extrapolation can be used to substantially reduce the PNO truncation error.[116,117] This is particularly important when using PNO energies to perform the complete basis set (CBS) extrapolation toward the basis set limit.

To illustrate the characteristics of the TURBOMOLE implementation and what is now possible, we report timings of PNO-CCSD(T) and PNO-CCSD(T)(F12*) calculations on a sequence of alkane chains and rock salt crystal fragments in Fig. 1. The default tight PNO truncation threshold was used in all cases. The def2-TZVPP basis was used for C_nH_{2n+2} and def2-TZVP for Na_nCl_n, respectively, and calculations were run on a 48-core Intel processor with 200 GB of memory. For the linear systems, the observed scaling is sub-quadratic, with $C_{128}H_{256}$ taking 15 h to complete. For the globular systems, the observed scaling is sub-cubic up to $Na_{50}Cl_{50}$, which takes 45 h to complete. The F12 calculations are two to three times more costly than non-F12 calculations but provide energies close to the basis set limit without requiring basis sets with a large number of AOs per atom.

Figure 2 gives example applications of DLPNO-CCSD(T) theory in organometallic chemistry in open- and closed-shell complexes involving Pd, Fe, and Cr metal centers with up to 90 atoms. Tight PNO thresholds were used in all cases. For unrestricted electronic states with low spin-contamination, the two- and three-body correlation and associated orbital relaxation captured in CCSD(T) theory provide accurate electronic energies at low computational expense. An equivalent treatment using multi-reference theory requires large double-shell active spaces to capture the orbital relaxation.

B. Periodic DLPNO-MP2

The computation of ground state properties of materials, such as structure, energies of cohesion, deformation energies, and surface interaction energies, poses a serious challenge to correlated wavefunction methods. Standard density-fitted MP2 theory scales as $O^2V^2XN_k^3$ where O, V, and X are the number of occupied, virtual, and auxiliary orbitals in the unit cell, and N_k are the number of k-points used to sample the Brillouin zone. This grows to $O^3V^4N_k^5$ for CCSD(T) theory. The near linear-scaling DLPNO scheme presents a solution to this challenge for insulators and semi-conductors, where the crystal orbitals can be localized so that local correlation methods can be applied to compute energies at the thermodynamic limit for sizable unit cells.

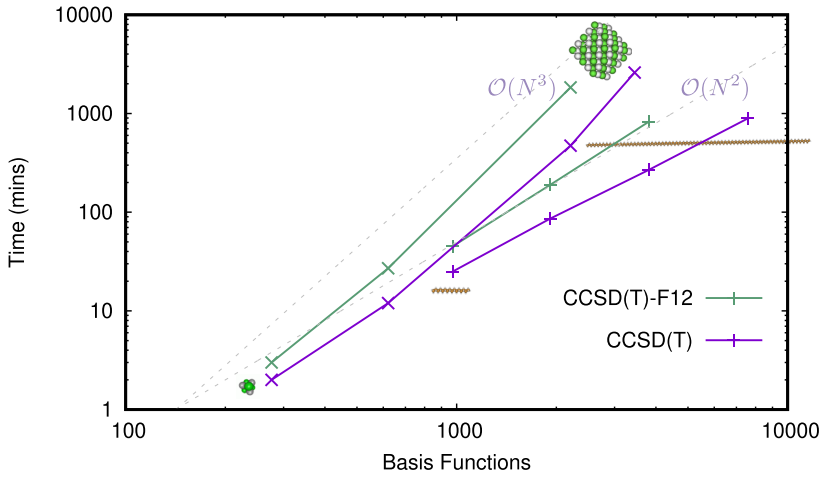


FIG. 1. Wall times for DLPNO-CCSD(T) and DLPNO-CCSD(T)-F12 calculations on C_nH_{2n+2} chains, and Na_nCl_n crystals using a triple-zeta basis and the default tight PNO truncation threshold. Sub-quadratic scaling emerges for globular systems with pairs separated by more than ~15 Å. Reprinted with permission from Franzke *et al.*, J. Chem. Theory Comput. **19**, 6859 (2023). Copyright 2023 Author(s), licensed under a Creative Commons Attribution CC BY 4.0 License.

12 November 2026 10:29:21

© Author(s) 2026

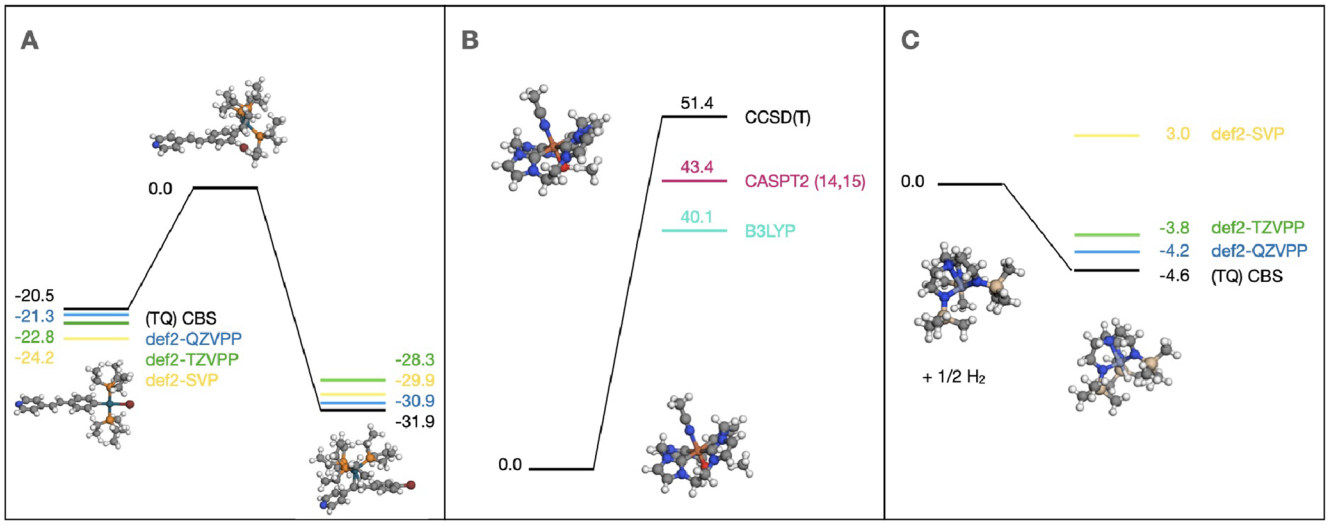


FIG. 2. (a) Forward and reverse DLPNO-CCSD(T) barrier heights for reaction 17 from the MOBH35 dataset.[117] (b) Hydrogen abstraction barrier for a high-valent Fe(IV)-oxo complex.[118] DLPNO-CCSD(T) calculations employed the scalar-relativistic X2C Hamiltonian and x2c-TZVPPall basis set. (c) DLPNO-CCSD(T) reaction energies for a 1-electron oxidative addition from the ROTS61 dataset.[119]

To this end, the DLPNO-MP2 method has been extended to handle periodic boundary conditions. The approach uses Gaussian AO basis sets and follows the Wannier function formulation of the MP2 equations. Starting from a RHF or UHF reference state for a Born–von Kármán (BvK) supercell, computed using the periodic Hartree–Fock implementation in `riper`,[120] well-localized Wannier functions are obtained through a periodic extension of the intrinsic bond orbital (IBO) localization procedure.[121,122] The second-order correlation energy per unit cell is evaluated as

$$E_{\mathrm{corr}} = \sum_{i_0 \leq j_\mathbf{l}} (2 - \delta_{i_0 j_\mathbf{l}}) \sum_{\tilde{a}\tilde{b} \in [i_0 j_\mathbf{l}]} (2 g^{\tilde{a}\tilde{b}}_{i_0 j_\mathbf{l}} - g^{\tilde{b}\tilde{a}}_{i_0 j_\mathbf{l}}) t^{i_0 j_\mathbf{l}}_{\tilde{a}\tilde{b}} + \Delta, \tag{20}$$

where $i_\mathbf{0}$ is an occupied Wannier orbital of the reference unit cell and $j_\mathbf{l}$ is an occupied Wannier orbital in the **l**th unit cell of the supercell. g and t are the electron repulsion integrals and the spin-free MP2 amplitudes, respectively. The domain of PNOs for each pair, $\tilde{a}\tilde{b} \in [i_\mathbf{0} j_\mathbf{l}]$, is determined by the user-defined PNO occupation number truncation parameter $\mathscr{T}$. The correction term Δ approximately accounts for the contribution from discarded pairs and PNOs. The first-order amplitudes are determined from the first-order coupled linear equations,

$$\begin{aligned} 0 = g^{i_0 j_\mathbf{l}}_{\tilde{a}\tilde{b}} + (\varepsilon_{\tilde{a}} + \varepsilon_{\tilde{b}}) t^{i_0 j_\mathbf{l}}_{\tilde{a}\tilde{b}} - \sum_{k_\mathbf{m}} \sum_{\tilde{c}\tilde{d} \in [k_\mathbf{m} j_\mathbf{0}]} S^{\tilde{c},k_\mathbf{m} j_\mathbf{0}}_{\tilde{a},i_{-1} j_\mathbf{0}} S^{\tilde{d},k_\mathbf{m} j_\mathbf{0}}_{\tilde{b},i_{-1} j_\mathbf{0}} t^{k_\mathbf{m} j_\mathbf{0}}_{\tilde{c}\tilde{d}} f^{i_\mathbf{0}}_{k_{\mathbf{m}+\mathbf{l}}} \\ - \sum_{k_\mathbf{m}} \sum_{\tilde{c}\tilde{d} \in [i_\mathbf{0} k_\mathbf{m}]} S^{\tilde{c},i_\mathbf{0} k_\mathbf{m}}_{\tilde{a},i_\mathbf{0} j_\mathbf{l}} S^{\tilde{d},i_\mathbf{0} k_\mathbf{m}}_{\tilde{b},i_\mathbf{0} j_\mathbf{l}} t^{i_\mathbf{0} k_\mathbf{m}}_{\tilde{c}\tilde{d}} f^{j_\mathbf{0}}_{k_{\mathbf{m}-\mathbf{1}}}, \end{aligned} \tag{21}$$

where S are the overlap matrices between the PNOs for two different pairs and f is the Fock matrix in the Wannier basis. This formulation fully exploits translational symmetry so that only quantities with one index in the reference cell are evaluated and stored. This formally leads to costs that scale linearly with the size of the unit cell and sublinearly with the number of unit cells in the supercell. Two modes of computation are available for periodic DLPNO-MP2 calculations: a BvK supercell treatment[123] and a megacell embedding treatment.[124]

1. BvK supercell treatment

In BvK mode,[123] the electron repulsion integrals are computed through chargeless density fitting and three-index integrals are evaluated through direct-space lattice summation with surface correction term,

$$(i_\mathbf{0} a_\mathbf{n} | Q_\mathbf{l})_{\mathrm{BvK}} = \sum_{\mathbf{LN}}^{\mathscr{M}} (i_\mathbf{0} a_{\mathbf{n}+\mathbf{N}} | Q_{\mathbf{l}+\mathbf{L}}) + S^{Q_\mathbf{l}}_{i_\mathbf{0} a_\mathbf{n}}, \tag{22}$$

with the auxiliary basis functions Q for the density fitting approximation. The integral evaluation can be greatly accelerated through the fast multipole approximations employed in the `riper` program, but this has not yet been implemented and, at the time of writing, the evaluation of the direct-space lattice summation to sufficiently large extent $\mathscr{M}$ remains a computational bottleneck. DLPNO-MP2 energies obtained using the BvK mode can be compared directly with canonical MP2 results for equivalent supercells. However, the megacell embedding treatment is much more efficient and is recommended for computing energies with large supercells to approach the thermodynamic limit.

2. Megacell embedding

The megacell approach[124] proceeds by first performing a HF calculation with a dense **k**-point mesh, corresponding to a large supercell, which is referred to as the megacell. The DLPNO-MP2 calculation is then performed on a smaller supercell embedded within the megacell. The correlation pair list $i_\mathbf{0} j_\mathbf{l}$ extends over the occupied Wannier functions within the embedded supercell, and the PAO and

12 November 2026 10:29:21

© Author(s) 2026

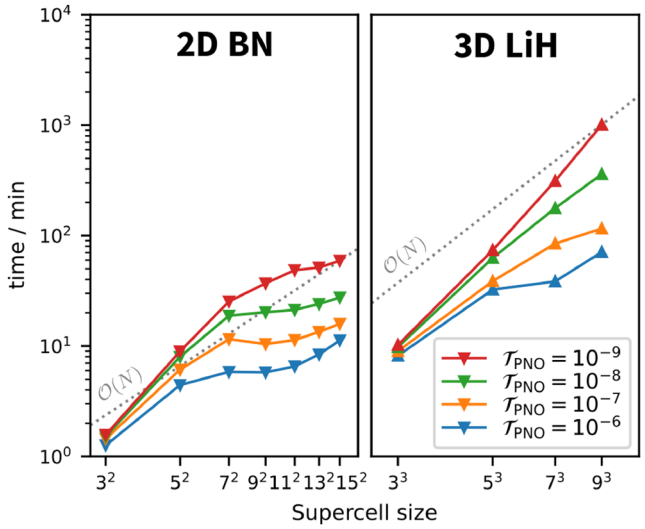


FIG. 3. Wall times for DLPNO-MP2 correlation energy calculations on BN sheets and LiH crystals using the pob-TZVP basis set. All calculations were executed on a single thread of an Intel(R) Xeon(R) Gold 6248R CPU with a maximum RAM limit of 386 GB. Reprinted with permission from Zhu *et al.*, J. Chem. Phys. **163**, 214108 (2025). Copyright 2025 Author(s), licensed under a Creative Commons Attribution CC BY-NC 4.0 License.

density fitting domains are restricted to within one supercell, centered around either one of the **0** or **l** lattice sites. The translational symmetry of the working equations imposes supercell periodicity on the correlation treatment. To ensure that there are no artifacts due to edge effects, the megacell should extend beyond the central supercell by at least half the supercell extent in every periodic direction. Since the integrals do not involve lattice sums, the megacell scheme is highly efficient.

Figure 3 reports timings for DLPNO-MP2/pob-TZVP calculations on 2D boron nitride and 3D lithium hydride. The most costly steps are the evaluation of the three-index integrals and the formation and diagonalization of the semi-canonical MP2 density. Since these steps scale sub-linearly with supercell size, for larger supercells, costs become dominated by linear-scaling steps, such as evaluating the differential overlap integrals used to determine local density fitting domains. An example application[125] of the DLPNO-MP2 method to the study of CO adsorption on MgO(001) is illustrated in Fig. 4. CO molecules at different coverage densities were placed on a 2-layer slab of pristine MgO. Counterpoise-corrected interaction energies were computed with the DLPNO-MP2 method with a 5×5 supercell, using a modified pob-TZVP-rev2 basis and a tight PNO threshold.

V. COMPLETE ACTIVE SPACE METHODS

A recent major extension of TURBOMOLE is the implementation of a complete active space configuration interaction (CAS-CI) method. Unlike conventional approaches, which are typically based on spin-free wave functions followed by spin–orbit coupling in a second step, the present implementation is able to employ two-component spinors and, thus, special relativity, including spin–orbit coupling from the beginning.[126] The wave function is expanded in the complete active space of Slater determinants generated from the selected active spinors,

$$|\Psi\rangle = \sum_{p}^{N_{\mathrm{det}}} C_p |\psi_p\rangle, \tag{23}$$

where the number of determinants is given by

$$N_{\mathrm{det}} = \binom{N_s}{n_e}, \tag{24}$$

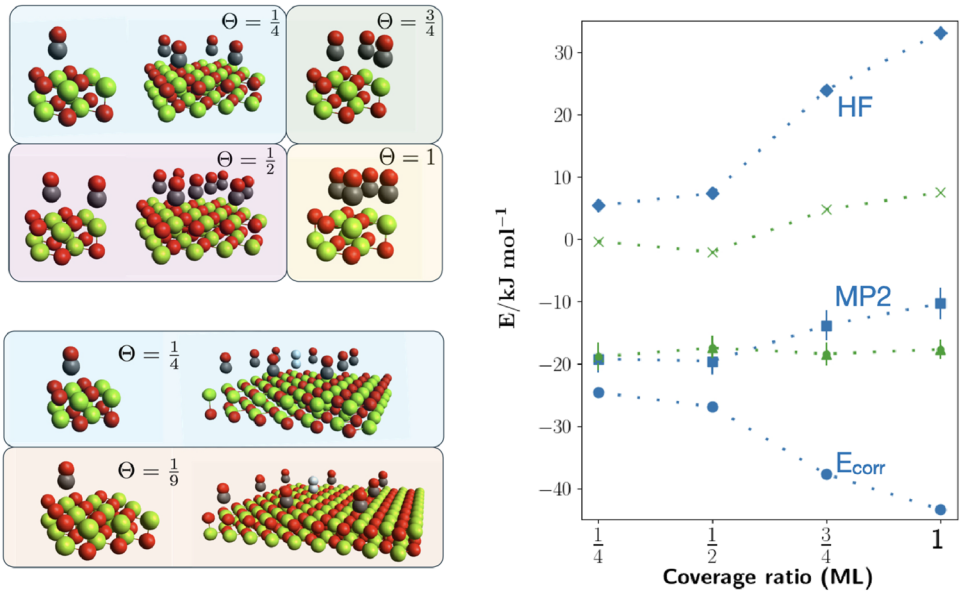


FIG. 4. Counterpoise-corrected DLPNO-MP2 interaction energies for CO on MgO(001) at low and dense coverages. The green crosses denote the contribution from lateral CO interactions, and green bells denote the DLPNO-MP2 energies neglecting these contributions. Adapted with permission from Zhu *et al.*, J. Chem. Theory Comput. **22**, 3927 (2026). Copyright 2026 Author(s), licensed under a Creative Commons Attribution CC BY 4.0 License.

12 November 2026 10:29:21

© Author(s) 2026

with the number of active spinors N_s and the number of electrons n_e. The CAS-CI Hamiltonian is, therefore, constructed and diagonalized directly in the determinant basis, providing a conceptually simple and efficient formulation in the two-component framework.

The implementation follows the integral-direct and density-fitting philosophy already established throughout TURBOMOLE.[16,30–34] Two-electron contributions are evaluated via RI intermediates rather than being stored as four-index integrals, keeping memory requirements moderate while fully exploiting the existing RI infrastructure.

Suitable reference spinors can be obtained from either Hartree–Fock or Kohn–Sham calculations including relativistic effects with the all-electron X2C Hamiltonian, while two-electron spin–orbit picture-change effects can be included approximately through (modified) screened nuclear spin–orbit (SNSO/mSNSO) corrections.[127–129] The CAS-CI energy is evaluated within the active space, thereby avoiding double counting of correlation effects,

$$E_{\mathrm{CAS-CI}} = E_{\mathrm{core}} + \langle \Psi | \hat{H}^{\mathrm{CAS}} | \Psi \rangle, \tag{25}$$

with the active-space Hamiltonian

$$\hat{H}^{\mathrm{CAS}} = \sum_{tu} h^c_{tu} \hat{E}_{tu} + \frac{1}{2} \sum_{tuvw} (tu|vw) \left(\hat{E}_{tu} \hat{E}_{vw} - \delta_{uv} \hat{E}_{tw} \right). \tag{26}$$

Here, indices $t, u, \ldots$ denote active spinors, h^c_{tu} contains the one-electron contribution and interactions with the inactive space, and $\hat{E}_{tu}$ are unitary group excitation operators.

This framework enables accurate calculations of atomic multiplet structures, crystal-field splittings, and field-dependent spectra, e.g., of open-shell lanthanide compounds. This is demonstrated in Fig. 5, where CAS-CI@CHYF excitation energies are compared to the atomic levels from the NIST database.[130] The clustering of low-energy states close to the diagonal demonstrates that the DFT-based CAS-CI reference captures the ground-term multiplet structure and low-lying spin–orbit splittings with good accuracy, whereas the increasing deviations at higher excitation energies indicate the growing importance of dynamic correlations outside the 4f active space.

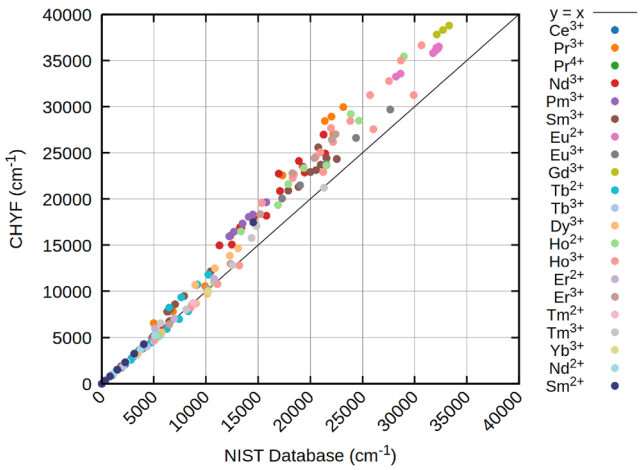


FIG. 5. Scatterplot of calculated atomic levels of 21 lanthanide ions at the CAS-CI@CHYF/x2c-QZVPPall-2c level with an mSNSO correction for X2C, plotted against reference atomic levels from the NIST database. The diagonal marks perfect agreement. Adapted with permission from Zielke, Weigend, and Holzer, Phys. Chem. Chem. Phys. **27**, 12284 (2025). Copyright 2025 Author(s), licensed under a Creative Commons Attribution CC BY 3.0 License.

This method further has also been applied to helium-tagged lanthanide antenna complexes, where CAS-CI@CHYF reproduced the Stark splitting pattern of the Yb^{3+}, $^2F_{7/2} \rightarrow {}^2F_{5/2}$ manifold,[131] and $YbPc_2$, where field-dependent CAS-CI calculations were used to simulate the Yb M_5-edge in x-ray absorption spectroscopy (XAS) and x-ray magnetic circular dichroism (XMCD) spectra.[132] Overall, the new complete active space functionality substantially broadens the applicability of TURBOMOLE to multireference methods for spectroscopy of heavy-element and strongly coupled spin–orbit systems.

Future developments will focus on extending this framework beyond the present CAS-CI capabilities. This includes an automatic active space builder to facilitate robust and reproducible active-space selections, restricted active-space (RAS) expansions for more flexible configuration spaces, EPR properties, linear response (LR) formulations, and the extension of the orbital-optimization machinery toward a more general CASSCF framework.

VI. SPECIAL RELATIVITY AND MAGNETISM

A. NMR shifts and spin–spin couplings

NMR spectroscopy is a key tool to characterize compounds and study the molecular geometry or electronic structure. In 2020,[3] TURBOMOLE provided NMR chemical shifts for non-relativistic and scalar-relativistic calculations[133–135] and non-relativistic NMR coupling constants.[63] Full relativistic treatments of NMR parameters, however, were not yet available, limiting the applicability of the program to light-element chemistry. This gap has been closed over the past five years by a series of major developments, namely the complete inclusion of relativistic effects,[106,136–142] current-dependent meta-GGAs,[10,95,96] as well as the modern local hybrid functionals[96,143,144] and the extension to open-shell systems for paramagnetic NMR based on the EPR tensors, which is separately described in Secs. VI B and VI C.[97,145,146] Overall, NMR spectra can now be accurately simulated throughout the periodic table of elements. These developments are accompanied by the extension toward superheavy elements up to Og[142] as well as the full two-component non-collinear extension of the Mulliken, Löwdin, and natural population analyses or the density of states to study the spin variables for EPR spectra[147] in both 1c and 2c approaches with the next release V8.1. Likewise, the Mayer bond indices are then available with spin–orbit coupling by using the symmetric spin densities and the antisymmetric current densities.[148] This allows to study both the chemical bonding and the magnetic properties with the full inclusion of relativistic effects.

For a closed-shell system, the indirect NMR spin–spin coupling tensor associated with the two nuclei N, M is directly available as a second-order property via

$$K^{NM}_{wu} = \frac{\mathrm{d}^2 E}{\mathrm{d}m_{M,u}\mathrm{d}m_{N,w}} = \mathrm{tr}\left(\mathbf{D} \frac{\partial^2 \mathbf{h}}{\partial m_{M,u} \partial m_{N,w}} \right) + \mathrm{tr}\left(\frac{\partial \mathbf{D}}{\partial m_{M,u}} \frac{\partial \mathbf{h}}{\partial m_{N,w}} \right), \tag{27}$$

12 November 2026 10:29:21

© Author(s) 2026

with the one-electron density matrix **D**, the one-electron Hamiltonian **h**, and the nuclear magnetic moments $\mathbf{m}_N$ and $\mathbf{m}_M$. This equation introduces the reduced coupling tensor K^{NM}_{wu}. The gyromagnetic ratio γ and Planck's constant h are then applied to convert it to the coupling tensor,

$$J^{NM}_{wu} = h\frac{\gamma_N}{2\pi}\frac{\gamma_M}{2\pi}K^{NM}_{wu}, \tag{28}$$

and the corresponding isotropic constant $J(N,M)$ in Hz. Likewise, the NMR shielding constant is given as the mixed second-derivative of the energy with respect to the magnetic field **B** and the nuclear magnetic moment $\mathbf{m}_N$ as

$$\sigma_{N,wu} = \frac{\mathrm{d}^2E}{\mathrm{d}B_u \mathrm{d}m_{N,w}} = \mathrm{tr}\left(\mathbf{D}\frac{\partial^2\mathbf{h}}{\partial B_u \partial m_{N,w}}\right) + \mathrm{tr}\left(\frac{\partial\mathbf{D}}{\partial B_u}\frac{\partial\mathbf{h}}{\partial m_{N,w}}\right). \tag{29}$$

NMR shifts δ are subsequently obtained with the isotropic shielding constant σ of a reference system and the sample as

$$\delta(N) = \sigma(\mathrm{ref}) - \sigma(N). \tag{30}$$

Both the unperturbed and the perturbed density term of NMR coupling and shielding tensors can be partitioned into a scalar and a spin–orbit contribution. The treatment of spin–orbit coupling in a variational two-component approach requires a complex framework for the SCF and the response part.[149] Especially for the response part, the inclusion of spin–orbit effects leads to structural changes of the equations and conceptual differences from the non-relativistic or scalar-relativistic *Ansatz*. To illustrate this, the contribution of the perturbed density matrix is rewritten as[139,150,151]

$$\mathrm{tr}\left(\frac{\partial\mathbf{D}}{\partial B_u}\frac{\partial\mathbf{h}}{\partial m_{I,w}}\right) = \sum_{\mu\nu}\frac{\partial\mathbf{h}_{\mu\nu}}{\partial m_{I,w}}\left(U^{B_u}_{\mu\nu} + V^{B_u}_{\mu\nu}\right), \tag{31}$$

where the occupied-virtual block of $\left\{\mathbf{U}^{B_u}, \mathbf{V}^{B_u}\right\}$ are the solutions of the coupled perturbed Kohn–Sham (CPKS) equation,

$$\begin{pmatrix}\mathbf{A} & \mathbf{B}\\ \mathbf{B}^* & \mathbf{A}^*\end{pmatrix}\begin{pmatrix}\mathbf{U}^B\\ \mathbf{V}^B\end{pmatrix} = \begin{pmatrix}\mathbf{P}^B\\ \mathbf{P}^{B,*}\end{pmatrix}, \tag{32}$$

with the perturbation $\mathbf{P}^B$. In a spin–orbit formalism, the CPKS equations always need to be solved iteratively—even for pure functionals—as spin–orbit coupling induces spin-current densities in the ground state. Then, the magnetic field acts as an imaginary perturbation and the spin-current densities give rise to a spin magnetization density and the associated exchange–correlation kernel in the CPKS equations.[139,150–152] Thus, the orbital rotation matrix on the left hand side of Eq. (32) is defined as

$$A_{ai,bj} = (\varepsilon_a - \varepsilon_i)\delta_{ij}\delta_{ab} + C_{ai,jb}, \tag{33}$$

$$B_{ai,bj} = C_{ai,bj}, \tag{34}$$

and **C** denotes the interaction kernel with the exchange–correlation kernel f^{XC} according to

$$C_{pq,rs} = (pq|rs) + f^{\mathrm{XC}}_{pq,rs} - c_{\mathrm{X}}(ps|qr). \tag{35}$$

In these equations, $(pq|rs)$ is a complex four-index two-electron integral in Mulliken notation. The standard index notation is applied. That is, i,j denotes occupied spinors and a,b denote virtual spinors. p,q,r,s are used for arbitrary spinors states. c_{X} indicates the fraction of the exact exchange, and ε_p are the spinor energy eigenvalues. We stress that NMR coupling constants are also obtained in an iterative procedure—even with pure functionals.[137,153]

Considering the increased complexity of the spin–orbit two-component approach, efficient and robust approximations are key to applicability to large systems. Therefore, the MARI-J and the seminumerical HF exchange (snK) approximations are combined with local X2C to compute the spectra of extended systems with hundreds of atoms using hybrid functionals in just a few hours or days. The errors introduced by MARI-J, snK, or local relativistic approximations, such as the diagonal local approximation to the unitary decoupling transformation (DLU), are negligible,[136–140] yet they lead to a drastic decrease of computation time and memory requirements as shown in Fig. 6.

Such robust approximations allow for a realistic simulation of NMR spectra, as demonstrated for the protonated form of the binary pseudo-tetrahedral Zintl anion $(HGe_3P)^{2-}$ in N,N-dimethylformamide (DMF).[155] According to DFT and coupled-cluster calculations, the hydrogen atom is placed on the Ge–Ge edge of the underlying (Ge_3P) skeleton and a three-center-two-electron bond is formed. All other structure motifs are disfavored by more than 40 kJ/mol and consequently irrelevant at room temperature.

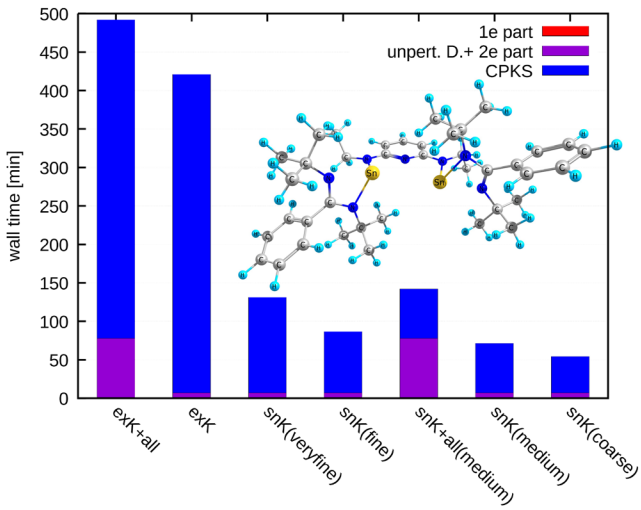


FIG. 6. Wall times in minutes for the calculation of the NMR shieldings of the tin pincer ligand $Sn_2N_7C_{39}H_{59}$ introduced in Ref. 154. The calculations were performed at the 2c spin–orbit DLU-X2C/PBE0/x2c-TZVPPall-2c level of theory with a central processing unit (CPU) of type AMD EPYC 7453 utilizing a total of 48 OpenMP threads. "+all" denotes that shieldings were calculated for all atoms, else only the two Sn were considered. snK denotes seminumerical HF exchange, and exK denotes analytical exact exchange. Computation times for the first-order magnetic-field X2C derivatives (1e part), the unperturbed density contribution, including the two-electron integrals of the CPKS right-hand side (unpert. D. + 2e part), as well as for the iterative CPKS procedure (CPKS), are listed. Adapted with permission from Y. J. Franzke and C. Holzer, J. Chem. Phys. **159**, 184102 (2023). Copyright 2023 Author(s), licensed under a Creative Commons Attribution CC BY 4.0 License.

12 November 2026 10:29:21

© Author(s) 2026

NMR experiments and computational simulations were carried out to confirm the structure; however, the initial theoretical studies were insufficient as solvent effects are of utmost importance for the ^{31}P NMR shifts and an explicit treatment of solvent molecules is necessary. Therefore, a solute–solvent system as depicted in Fig. 7 was constructed and then the NMR properties are reproduced in excellent agreement with the experiment as shown in Table IV. Spin–orbit coupling only affects the ^{31}P shielding constants but not the ^{31}P shift. In contrast, a small but notable spin–orbit heavy on the light atom (SO-HALA) effect of about 2 ppm is observed for the hydrogen shift. Here, the inclusion of spin–orbit effects is mandatory for a quantitative agreement with the experiment. Of course, the two-component formalism is also applicable to systems with much stronger SO-HALA effects,[156,157] such as selenocyanate and tellurocyanate anions, where spin–orbit coupling changes the ^{13}C NMR shifts by 21.8 and 64.9 ppm, respectively.[156] Therefore, our implementation allows to accurately study the complete periodic table of elements.

B. EPR properties

Open-shell species are routinely characterized with EPR spectra. Over the last five years, their calculation using relativistic density functional methods has been implemented in TURBOMOLE. Like the NMR properties, the EPR g-tensor $\boldsymbol{g}$ and the electron–nucleus hyperfine coupling tensor $\boldsymbol{A}$ are formally second-order properties defined with the mixed derivatives with respect to the spin and the magnetic field or nuclear spin, which is related to the nuclear magnetic moment. However, these tensors can be evaluated as first-order properties in a spin–orbit two-component framework with

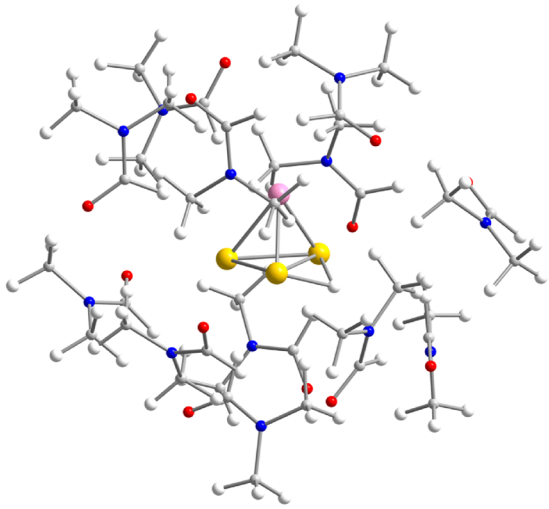


FIG. 7. One optimized structure of the Zintl anion $(HGe_3P)^{2-}$ surrounded by 12 DMF solvent molecules, which represents the basis for the calculated NMR shifts in solution. Three different solvent–solute structures are considered to estimate the effect of molecular dynamics. An initial solute–solvent system was constructed with CREST[158] and subsequently optimized at the scalar DLU-X2C/TPSS-D3(BJ)/x2c-TZVPall-s/COSMO level. Atom color code: Ge: yellow, P: rose, C: gray, N: blue, O: red, H: white. Reprinted with permission from Spang *et al.*, ChemRxiv (2026), DOI: 10.26434/chemrxiv.10002006/v3 Copyright 2026 Author(s), licensed under a Creative Commons Attribution CC BY 4.0 License.

TABLE IV. NMR properties of $(HGe_3P)^{2-}$ in DMF at the scalar (SR) and spin–orbit (SO) DLU-X2C/TPSS/x2c-TZVPall-s/COSMO level. The calculations are performed with COSMO to account for solvent effects or with 12 explicit DMF solvent molecules. For the latter, COSMO is additionally applied for the long-range effects, i.e., a cavity around the whole system was constructed. Shifts δ are given in ppm and ^2J coupling constants in Hz. Data taken from Ref. 155. The Boltzmann average is formed for the solute–solvent systems.

	$\delta(^1\mathrm{H})$	$\delta(^{31}\mathrm{P})$	^2J (^{1}H, ^{31}P)
SR-X2C, COSMO-only	−8.75	−569.8	8.2
SO-X2C, COSMO-only	−11.28	−570.6	7.1
SR-X2C, DMF + COSMO	−7.62	−431.4	7.9
SO-X2C, DMF + COSMO	−9.82	−431.3	6.9
Experiment in DMF	−10.03	−432.9	3.9

three independent non-collinear calculations, where the magnetization is aligned along three orthogonal directions.[159] This approach is implemented at the X2C level with functionals supported up to (current-dependent) local hybrid functionals.[160,161] For analysis purposes, it is also possible to decouple the two-component HFC into the Fermi-contact, spin–dipole, paramagnetic spin–orbit, and a purely relativistic term.[162] This allows to directly study the impact of spin–orbit effects and the density in the vicinity of the nuclei. The accuracy of one-electron X2C was assessed for a set of transition-metal complexes, and here, the calculated EPR properties differ by about 4% from the four-component Dirac–Kohn–Sham reference results. With the mSNSO approximation,[127,163] this is reduced to less than 0.5%.[160,161] Therefore, X2C accurately captures all relevant relativistic effects.

As an approximation, a spin–orbit perturbation theory framework is available for both tensors. Here, the scalar Fermi-contact and spin–dipole terms of the HFC can directly be evaluated from the ground-state density matrix at the DFT, RPA, or coupled-cluster level.[145,164] The paramagnetic spin–orbit term is available from the response density with respect to the spin–orbit perturbation in DFT.[97]

Typically, the two-component SCF procedure requires a large number of SCF iterations. To solve this issue, the canonical non-collinear formalism[22,23,106,107,165,166] was complemented by an implementation of the non-collinear Scalmani–Frisch approach for increased numerical stability.[108,167–169] Here, the regularized version suggested by Komorovsky *et al.* for GGAs[168] was generalized to meta-GGAs and local hybrid functionals. In case of vanishing spin auxiliary quantities, the corresponding collinear limit or the closed-shell limit is explicitly formed. Together with complex generalized DIIS and automatic level shifting, this drastically reduces the number of SCF iterations and allows for a smooth convergence behavior.

The capability of the EPR features is illustrated by applications to Lu^{2+} single molecule magnets in the context of molecular qubits.[147,160,161,170] These systems with large hyperfine coupling constants are so-called clock quubits with long decoherence times.[171] A large hyperfine coupling constant is most easily found when the Fermi-contact term is dominating due to a large s-parentage. Therefore, bent metallocenes in axial symmetry as shown in Fig. 8 are considered, as this allows for a large admixture of the 6s and

12 November 2026 10:29:21

© Author(s) 2026

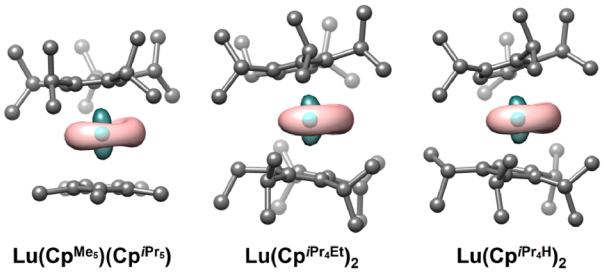


FIG. 8. Molecular structure of the three Lu^{2+} single molecule magnets $Lu(Cp^{i}Pr_4H)_2$, $Lu(Cp^{i}Pr_4Et)_2$, and $Lu(CpMe_5)(Cp^{i}Pr_5)$ denoted **1–3** in a pseudo-^2S ground state. Hydrogen atoms are omitted for clarity. Atom color code: C gray and Lu green. The singly occupied molecular orbitals (SOMOs) corresponding to the Lu compounds **1–3** are shown at an isosurface value of 0.07. The SOMOs are of $5d_{z^2}$ – 6s hybrid character. Reprinted with permission from Ngo *et al.*, J. Am. Chem. Soc. **147**, 13799 (2025). Copyright 2025 Author(s), licensed under a Creative Commons Attribution CC BY-NC-ND 4.0 License.

the $5d_{z^2}$ orbitals at the Lu center in a doublet ground state.[147] The EPR parameters are collected in Table V and show that the hyperfine coupling constant increases with increasing Cp–Lu–Cp bent angle. Likewise, the g-tensor is nearly isotropic and close to 2. Overall, increasing axial symmetry leads to a rise of the 6s parentage as evident from a natural population analysis and the Morton–Preston approach[172] to the isotropic hyperfine coupling. The latter is applicable due to the dominating Fermi-contact term and the scalar-relativistic effects. For systems with strong spin–orbit effects, the Morton–Preston approach leads to a notable deviation from quantum-chemical population analyses, as the approximations introduced by the Morton–Preston *Ansatz* are no longer reliable.[173]

Starting with triplet systems, spin–orbit and spin–spin coupling lifts the degeneracy of the M_S sublevels. For instance, the three sublevels of a triplet in axial symmetry split into $M_S = 0$ and $M_S = \pm 1$ states. Here, the transitions from $M_S = 0$ to $M_S \pm 1$ *et* vice versa are allowed spin transitions. Consequently, this zero-field splitting (ZFS) leads to more complicated EPR spectra and is an important quantity for the magnetic characterization. TURBOMOLE offers an efficient relativistic DFT approach for the full ZFS tensor,[98]

$$D_{uw} = D_{uw}^{\mathrm{SD}} + D_{uw}^{\mathrm{SO}}, \tag{36}$$

consisting of a spin–dipole term D_{uw}^{SD} with the unperturbed electron density[174] and a spin–orbit contribution D_{uw}^{SO} in a CPKS scheme,

$$D_{uw}^{\mathrm{SO}} = D_{uw}^{\mathrm{SO},\alpha} + D_{uw}^{\mathrm{SO},\beta} - D_{uw}^{\mathrm{SO},\alpha\beta} - D_{uw}^{\mathrm{SO},\beta\alpha}, \tag{37}$$

where the same-spin and the spin-flip contribution both arise from the response to a spin–orbit perturbation.[175] This spin–orbit perturbation is available within a non-relativistic and the X2C framework for all functionals up to (current-dependent) local hybrids.[98] Here, the axial ZFS parameter D, the rhombic parameter E, and the rhombicity parameter E/D are defined with elements of the ZFS tensor in its diagonal form according to

$$D = D_{zz} - \frac{1}{2}(D_{xx} + D_{yy}), \tag{38}$$

$$E = \frac{1}{2}(D_{xx} - D_{yy}), \tag{39}$$

$$0 \le E/D \le 1/3, \tag{40}$$

for a comparison with the experimental measurements.[176]

Main group compounds can exhibit extremely large zero-field splitting constants so that these systems behave as "non-magnetic" or diamagnetic triplet systems as demonstrated for triplet stibinidenes and bismuthinidenes stabilized by hydrindacene ligands.[177–180] Sb or Bi form a single σ-bond with the neighboring C atom and both non-bonding p orbitals at the pnictogene atom are singly occupied. The systems are of effective axial symmetry, and thus, the ZFS parameter E vanishes. Relativistic DFT results for ZFS and g-tensor of the triplet stibinidene hydrindacene molecule of Ref. 177 are presented in Table VI. The giant ZFS parameter D describes the energetic splitting of the magnetic sublevels into a thermally isolated $M_S = 0$ state and two excited $M_S = \pm 1$ states. Such a large splitting makes measurements of EPR spectra impossible, and the compound behaves similar to a diamagnetic system. Consequently, the g-tensor cannot be accurately determined in the experiment and two different fits are reported. Overall, the ZFS parameter D is only slightly dependent on the g-tensor in the experimental fitting procedures. As shown by the computational results, the isotropic g-tensor is close to the estimated range and the ZFS parameter is reproduced in very good agreement. Thanks to the low computational cost of DFT, the full molecule can be considered herein with large basis sets and no truncation of the ligand is needed. This demonstrates that modern DFT methods can be applied to the ZFS of axial systems with good accuracy.

TABLE V. EPR properties and s-parentage of the SOMO with spin–orbit DLU-X2C/ωB97X-D and triple-zeta basis sets for the three Lu single molecule magnets shown in Fig. 8 and the trigonal pyramidal $[Lu(N(SiMe_3)_2)_3]^-$. For the three bent sandwich metallocene complexes 1–3, the Cp–Lu–Cp bent angle ∠ is given in degree. The s-parentage is obtained from a natural population analysis of the SOMO at the DFT level and the Morton–Preston approach for the isotropic HFC. Computational (Calc.) and experimental (Expt.) Data are collected from Refs. 147, 160, 161, and 170.

	$[Lu(N(SiMe_3)_2)_3]^-$	Lu 1	Lu 2	Lu 3
Cp–Lu–Cp ∠	⋯	152.6°	157.0°	159.9°
g_{iso} Expt.	1.927	1.987	1.989	1.987
g_{iso} Calc.	1.917	1.991	1.992	1.989
A_{iso} Expt. (GHz)	2.44	4.17	4.30	4.38
A_{iso} Calc. (GHz)	2.38	4.18	4.28	4.34
s (Morton–Preston)	23.0%	39.2%	40.5%	41.2%
s (natural population)	28.6%	41.7%	42.7%	43.3%

C. Paramagnetic NMR shifts

The NMR spectra of open-shell systems are much more complicated than those of closed-shell diamagnetic systems. This is true for both the experimental measurements and interpretation due to large pseudo-contact shifts and line-broadening as well as their computational simulation. The latter require a balanced treatment of static and dynamic correlation as well as relativistic and

12 November 2026 10:29:21

© Author(s) 2026

TABLE VI. Zero-field splitting parameters D and E (in cm^{-1}) as well as the isotropic EPR g-tensor for the triplet stibinidene of Ref. 177. The structure of the single-crystal x-ray diffraction experiment was employed, and calculations were performed at the DLU-X2C/DFT/x2c-QZVPall-2c-s(Sb)/x2c-TZVPall-2c(C,H) level with the mSNSO(Hamiltonian) approximation. The isotropic g-tensors were obtained with either one-component spin–orbit perturbation theory (1c SOPT) or the non-collinear two-component spin–orbit (2c SO) approach. GIAOs were applied for all g-tensor calculations except for those with 2c SO CHYF, where a common gauge origin at the Sb atom was applied. The current-dependent generalization of τ was constructed for CHYF and the regularized 2c Scalmani–Frisch approach is used.

	ZFS		g_{iso}	
	D	E	1c SOPT	2c SO
PBE	880.1	0.1	2.018	1.873
B3LYP	1175.0	0.1	2.018	1.828
CHYF–B95	1259.2	0.2	2.019	1.840
Experiment (fixed g_{iso} = 2.00)	1030	0	2.00	
Experiment (fixed g_{iso} = 1.90)	930	0	1.90	

environmental effects. Consequently, different methodologies and computational frameworks are combined to simulate the spectra of a single compound. Generally, the paramagnetic NMR (pNMR) shielding tensor is the sum of the orbital shielding contribution, which is the straightforward open-shell generalization of Eq. (29), and a temperature-dependent term according to[181]

$$\boldsymbol{\sigma}_I^{\mathrm{tot}} = \boldsymbol{\sigma}_I^{\mathrm{orb}} + \boldsymbol{\sigma}_I^{\mathrm{temp}} = \boldsymbol{\sigma}_I^{\mathrm{orb}} - \frac{10^6 h\mu_e}{g_N \mu_I k_B T} \boldsymbol{A}_I \cdot \boldsymbol{Z} \cdot \boldsymbol{g}^{\mathrm{T}}, \tag{41}$$

using the (3×3) matrix[182]

$$Z_{kl} = \frac{1}{Q} \sum_{\lambda} e^{-\frac{E_\lambda}{k_B T}} \left[\sum_{aa'} \langle S\lambda a | \hat{S}_k | S\lambda a' \rangle \langle S\lambda a' | \hat{S}_l | S\lambda a \rangle \right.$$
$$\left. + 2k_B T \, \Re \sum_{\lambda' \neq \lambda} \sum_{aa'} \frac{\langle S\lambda a | \hat{S}_k | S\lambda' a' \rangle \langle S\lambda' a' | \hat{S}_l | S\lambda a \rangle}{E_{\lambda'} - E_\lambda} \right], \tag{42}$$

with the eigenvalues E_λ of the ZFS Hamiltonian $\hat{\mathbf{S}} \cdot \boldsymbol{D} \cdot \hat{\mathbf{S}}$. For clarity, operators are explicitly indicated for the spin S. Furthermore, λ and a denote the $(2S + 1)$ eigenfunctions, where a refers to the components of degenerate states, and Q indicates the partition function, $Q = \sum_{\lambda a} \exp\left[-E_\lambda/(k_B T)\right]$. The other constants in the equations are the nuclear g-factor g_I, the electron and nuclear magnetons μ_e and μ_I, as well as Boltzmann's constant k_B and the temperature T. For a doublet system, the pNMR tensor reduces to

$$\boldsymbol{\sigma}_I^{\mathrm{tot}} = \boldsymbol{\sigma}_I^{\mathrm{orb}} + \boldsymbol{\sigma}_I^{\mathrm{temp}} = \boldsymbol{\sigma}_I^{\mathrm{orb}} - \frac{10^6 h\mu_e}{g_I \mu_I} \frac{S(S+1)}{3k_B T} \boldsymbol{A}_I \cdot \boldsymbol{g}^{\mathrm{T}}. \tag{43}$$

Overall, all individual tensors or matrices can be evaluated in TURBOMOLE[146] and the total pNMR shielding tensor is subsequently assembled with the PNMRShift program.[183–185]

The challenges for pNMR are illustrated for the ^{1}H shifts of the three-coordinate Mo(III) complex Mo[N(R)Ar]$_3$ with $S = 3/2$ displayed in Fig. 9. The experimental spectra consist of four different shifts associated with the *t*Bu, *o*-ArH, $ArCH_3$, and *p*-ArH groups.

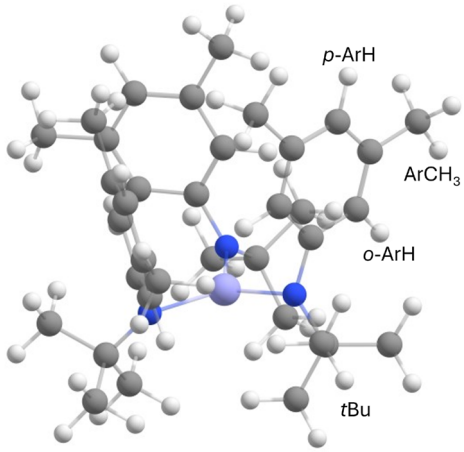


FIG. 9. Molecular structure of Mo[N(*t*Bu)Ar]$_3$ with $S = 3/2$ and labels for the ^{1}H pNMR. Atom color code: H: white, C: gray, N: blue, Mo: light blue. *o*-ArH and *p*-ArH refer to the ortho and para positions of the aryl group, respectively.

TABLE VII. ^{1}H pNMR chemical shifts (in ppm) of Mo[N(*t*Bu)Ar]$_3$ with $S = 3/2$ at 298 K relative to TMS with the DLU-X2C/x2c-QZVPall-s/COSMO(benzene) level. See Fig. 9 for the labels of the hydrogens. The computational and experimental data in benzene are taken from Refs. 146 and 186, respectively. The current-dependent generalization of τ was constructed for TPSS and LH20t. The experimental pNMR shifts were recorded with benzene as secondary reference.

	*t*Bu	*o*-ArH	$ArCH_3$	*p*-ArH
PBE	87.0	−35.4	−15.3	−87.2
TPSS	83.9	−48.9	−24.5	−88.3
LH20t	87.5	−26.8	−17.7	−63.1
Experiment	64.0	~ 23	−9.63	−51.67

According to Table VII, three of the four calculated shifts are in good agreement with the experiment. Here, the *t*Bu and *p*-ArH groups can easily be assigned to the pNMR shifts without the need to consider the integrals of the signals. For the signal of *o*-ArH, the incorrect sign is obtained. The orbital shift is about 6 ppm, and the incorrect sign can be attributed to a wrong sign and the wrong absolute value of the Fermi-contact term of the HFC. Accurate results for the HFC of the hydrogens are even more difficult to obtain, as the spin density is often very small, but it still leads to notable changes of the pNMR shifts. Furthermore, results are strongly dependent on the choice of the functional, which seriously limits the predictability of spectra. Multireference methods can be applied for the ZFS and the g-tensor, and, in principle, for HFC as well. However, their use is often limited by the need of large active spaces. Furthermore, it is not given that they always lead to a better description of the spin density, particularly at the positions of the nuclei, which is usually the most decisive factor for paramagnetic NMR.

D. Finite magnetic fields

So far, the magnetic field was treated as a perturbation for NMR and EPR spectroscopy. That is, the properties are calculated

12 November 2026 10:29:21

© Author(s) 2026

in the limit of a vanishing external magnetic field. However, TURBOMOLE can also perform efficient molecular non-relativistic[187,188] and relativistic calculations[189] with finite magnetic fields or strong magnetic fields of more than 1000 T. This is currently implemented at the HF,[187] CDFT,[105,108,190,191] *GW*-BSE,[192,193] RPA,[194] and CC2 levels[193] with London orbitals for gauge invariance. Consequently, it allows us to study ground and excited states in the presence of finite magnetic fields in the context of new types of chemical bonding or spin-phase transitions[195,196] as well as the Berry curvature.[197,198]

The recently developed X2C approach for finite magnetic fields[189] can be applied to compute the XMCD spectra of heavy elements in a proof-of-principle fashion.[132]

VII. EXCITED-STATE METHODS

A. TDDFT: Hybrid 2c TDDFT and damped response

Optical spectra are routinely analyzed and interpreted with linear response TDDFT (LR-TDDFT). Here, a non-relativistic approach is often sufficiently accurate for organic or inorganic compounds consisting of light elements only. For systems with transition-metal or heavier main-group elements, spin–orbit coupling may, however, lead to the splitting of peaks and is key for many photochemical processes. This is of importance for optical devices and technologies, such as organic light emitting diodes (OLEDs) or dye-sensitized solar cells (DSSCs) with hybrid perovskites. At the time of the previous review,[3] TURBOMOLE supported spin–orbit two-component TDDFT with semilocal GGAs[199,200] and hybrids within the Tamm–Dancoff approximation.[201] For full 2c hybrid TDDFT, only an initial implementation with GGA-based functionals was available.[15] This framework was subsequently thoroughly generalized to all DFT levels,[106,149] and the efficiency was vastly improved.[9,141] The full two-component LR-TDDFT equations with the Hermitian matrix $\mathbf{A}$ and the complex symmetric matrix $\mathbf{B}$ read

$$\begin{pmatrix} \mathbf{A} & \mathbf{B} \\ \mathbf{B}^* & \mathbf{A}^* \end{pmatrix} \begin{pmatrix} \mathbf{X} \\ \mathbf{Y} \end{pmatrix} = \omega \begin{pmatrix} \mathbf{1} & \mathbf{0} \\ \mathbf{0} & -\mathbf{1} \end{pmatrix} \begin{pmatrix} \mathbf{X} \\ \mathbf{Y} \end{pmatrix}, \tag{44}$$

and the orbital rotation matrices are defined as in Eqs. (33) and (34). $\mathbf{X}$ and $\mathbf{Y}$ are the solution vectors describing the excitation or de-excitation. Due to the high computational costs of the exact exchange contribution in full 2c hybrid TDDFT calculations, the seminumerical exchange approximation[9] or the RI exchange (RI-K) approximation[15,141] is essential for large-scale applications. The latter is highly efficient for the simultaneous treatment of many excited states but requires tailored auxiliary basis sets.[32]

The linear response approach is well suited for excitations associated with the valence region and a low or moderate density of states such as in organometallic systems. However, large metal clusters usually feature a high density of states. This consequently increases the number of excitations to be considered. That is, a large number of solutions are required for a small spectral region. Then, a damped response formalism[202] becomes advantageous and is implemented at all DFT levels.[149] Here, the CPKS response equations are essentially modulated with complex frequencies ω according to

$$\left[\begin{pmatrix} \mathbf{A} & \mathbf{B} \\ \mathbf{B}^* & \mathbf{A}^* \end{pmatrix} - \omega \begin{pmatrix} \mathbf{1} & \mathbf{0} \\ \mathbf{0} & -\mathbf{1} \end{pmatrix} \right] \begin{pmatrix} \mathbf{X} \\ \mathbf{Y} \end{pmatrix} = \begin{pmatrix} \mathbf{P}^{\nu} \\ \mathbf{P}^{\nu,*} \end{pmatrix}, \tag{45}$$

where $\mathbf{P}^{\nu}$ denotes the ν-component of the electric dipole integrals in the occupied-virtual space. Unlike linear response TDDFT, damped response TDDFT is intrinsically complex—even in the absence of spin–orbit coupling. Therefore, it is computationally more expensive than the linear response TDDFT approach in a non-relativistic or scalar-relativistic framework for a low density of states.

Based on the input for the frequency in damped response calculations, it is possible to choose an energy region of interest and a convoluted spectrum is evaluated from the polarizabilities at the complex frequency. This makes the damped response *Ansatz* an excellent choice for the calculation of core-level spectra, such as K or L edges in XAS. Here, it can validate the accuracy of the computationally cheaper core-valence separation (CVS) approach,[203] which simply freezes all occupied orbitals or spinors but the ones for the given edge in XAS. Consequently, the CVS LR-TDDDFT framework neglects the coupling between the valence and the core-excited states and this error is often unknown but can be rigorously assessed within the damped response framework.[204]

B. Real-time TDDFT

The RT-TDDFT implementation provides access to the non-equilibrium electron dynamics of molecular systems by directly propagating the time-dependent KS (TDKS) equations. In atomic units, the TDKS equations read

$$\mathrm{i}\frac{\partial}{\partial t}\psi_p(\mathbf{r},t) = \left[-\frac{1}{2}\nabla^2 + v_{\mathrm{eff}}[\rho(\mathbf{r},t)]\right]\psi_p(\mathbf{r},t), \tag{46}$$

where v_{eff} denotes the time-dependent effective KS potential, consisting of the external, Hartree, and XC contributions. The electron density is constructed from the occupied orbitals ψ_i as

$$\rho(\mathbf{r},t) = \sum_i f_i |\psi_i(\mathbf{r},t)|^2, \tag{47}$$

where f_i denotes the occupation number. Within a finite basis representation, the time evolution is most conveniently expressed in terms of the density matrix $\mathbf{D}(t)$, whose dynamics is governed by the von-Neumann equation,

$$\mathrm{i}\frac{\partial \mathbf{D}(t)}{\partial t} = [\mathbf{F}(t), \mathbf{D}(t)], \tag{48}$$

with the time-dependent KS matrix $\mathbf{F}(t)$. External electric fields are included within the dipole approximation, resulting in an additional time-dependent one-electron contribution to $\mathbf{F}(t)$. Time propagation is performed using unitary schemes (e.g., Magnus expansions), ensuring idempotency of the density matrix.

In contrast to LR-TDDFT, RT-TDDFT naturally captures non-linear effects, strong-field phenomena, and ultrafast electron dynamics. Spectroscopic observables are obtained from the Fourier transform of time-dependent response properties, such as the induced dipole moment.

Within RT-TDDFT, the density matrix becomes complex during time propagation. For local and semilocal XC approximations up to GGAs, the XC potential depends only on the electron density and its gradients and, therefore, only on the real symmetric part of the density matrix. Consequently, these functionals are unaffected by the imaginary components arising during time evolution. In contrast, meta-GGAs depend additionally on the kinetic-energy density

12 November 2026 10:29:21

© Author(s) 2026

τ. Early implementations employed this quantity in its standard, current-independent form.[205] However, the imaginary antisymmetric part of the density matrix gives rise to the particle current density $\mathbf{j}(\mathbf{r},t)$, which must be accounted for to ensure gauge invariance in time-dependent settings. This leads to a generalized kinetic-energy density,[7]

$$\tilde{\tau}(\mathbf{r},t) = \tau(\mathbf{r},t) - \frac{|\mathbf{j}(\mathbf{r},t)|^2}{2\rho(\mathbf{r},t)}. \tag{49}$$

Recently, the RT-TDDFT framework has been extended to fully incorporate current-dependent meta-GGAs as well as hybrid and range-separated hybrid functionals.[5] In the latter case, the time-dependent exact-exchange contribution naturally depends on the complex density matrix, placing hybrid functionals on the same formal footing as current-dependent meta-GGAs within RT-TDDFT and vice versa.

Overall, RT-TDDFT in TURBOMOLE combines efficient time propagation schemes with support for local, semi-local, current-dependent meta-GGAs and (range-separated) hybrid functionals, thereby enabling accurate simulations of ultrafast electronic processes in molecular systems.[5,205,206]

C. *GW*-BSE: Contour deformation, time-reversal symmetry breaking, non-linear response, magnetic fields

The recent *GW*-BSE-related works that have taken place in TURBOMOLE show a clear transition from using the Bethe–Salpeter equation mainly as an excitation energy method toward a general response-theory framework for molecular properties. Three contributions are particularly important in this direction: the extension of post-Kohn–Sham *GW* and RPA methods to time-reversal-symmetry-breaking references,[194] the formulation of non-linear light–matter interactions from the BSE,[207] and the recent overview that places these developments into the broader context of molecular properties from *GW*-BSE.[208]

The work on time-reversal-symmetry-breaking references is a key technical milestone because it removes an important restriction of many practical *GW*, RPA, and BSE implementations. Standard molecular implementations often assume real orbitals and time-reversal symmetry. This assumption fails in systems with magnetic fields, spin–orbit coupling, non-collinear spin structures, or complex-valued London orbitals. We showed how reduced-scaling auxiliary-subspace algorithms for RPA correlation energies and the correlation part of the *GW* self-energy can be generalized to complex Kohn–Sham references.[194] Conceptually, this is important because the quasiparticle correction,

$$\varepsilon_p^{\mathrm{QP}} = \varepsilon_p^{\mathrm{KS}} + Z_p\langle p|\Sigma^{\mathrm{X}} + \Sigma^{\mathrm{C}}(\varepsilon_p^{\mathrm{QP}}) - v_{\mathrm{XC}}^{\mathrm{KS}}|p\rangle, \tag{50}$$

must remain well defined even when the underlying orbitals are complex and time-reversal symmetry no longer simplifies the response structure. This development, therefore, provides the formal and algorithmic basis for applying *GW*-BSE to magnetically perturbed and relativistic open-shell molecular systems. It also connects naturally to earlier work on *GW*-BSE in magnetic fields and two-component relativistic *GW*-BSE.[15,149,193,204]

The recent non-linear BSE work represents a second major step: it turns *GW*-BSE from a primarily linear-response method into a tool for non-linear optical spectroscopy. Starting from the static-screened exchange approximation to the BSE kernel, the authors derived analytic expressions for quadratic response properties. In practice, this enables the calculation of the dynamic first hyperpolarizability and two-photon absorption strengths within a *GW*-BSE framework. The essential object is no longer only the first-order transition density associated with a BSE excitation but also a second-order response density that couples two external perturbations, schematically

$$\gamma^{(2)}(\omega_1,\omega_2) = \mathscr{R}_{\mathrm{BSE}}(\omega_1+\omega_2)\,\mathscr{K}^{(2)}\left[\gamma^{(1)}(\omega_1),\gamma^{(1)}(\omega_2)\right], \tag{51}$$

where $\mathscr{R}_{\mathrm{BSE}}$ denotes the BSE response resolvent and $\mathscr{K}^{(2)}$ collects the effective quadratic coupling terms. The practical significance is that non-linear observables can be obtained with machinery closely related to ordinary BSE response equations. The reported benchmarks are especially encouraging: with suitable Kohn–Sham starting points, *GW*-BSE gives first hyperpolarizabilities and two-photon absorption strengths with an accuracy comparable to coupled-cluster singles and doubles, while outperforming both second-order coupled-cluster and TDDFT for the tested small molecules.[207]

A closely related recent development is the extension of BSE response theory to state-to-state transitions and spin–orbit effects.[209] This work gives access to excited-state absorption, excited-state circular dichroism, and excited-state optical rotation from *GW*-BSE using second-order transition densities. It also derives fully relaxed perturbative spin–orbit coupling matrix elements within the *GW*-BSE framework. Together with the non-linear-response work, this broadens the method from ground-state absorption spectra to time-resolved and excited-state spectroscopies, where the relevant quantities are transitions between excited states rather than only from the ground state.

Overall, recent *GW*-BSE work in TURBOMOLE can be viewed as a systematic expansion along three axes. First, the time-reversal-symmetry-breaking work extends the domain of applicability to complex, magnetic, and relativistic references. Second, the non-linear BSE formulation extends the order of response from linear spectra to hyperpolarizabilities and two-photon processes. Third, TURBOMOLE consolidates these advances into a broader vision: *GW*-BSE as a general molecular-property method rather than merely a tool for excitation energies. The remaining challenges are also clear. The dependence on the *GW* starting point, the neglect or approximation of higher-order kernel derivatives, the treatment of dynamical screening, and the development of analytic gradients remain active areas. Nevertheless, the trajectory is compelling: *GW*-BSE is becoming an increasingly versatile, physically grounded alternative to TDDFT for molecular spectroscopy and response theory.

D. T-matrix formalism for light–matter interaction

The linear transfer matrix (T-matrix)[210] and its non-linear counterpart hyper-T-matrix approaches provide a compelling framework for connecting molecular quantum chemistry with mesoscopic optical scattering simulations. In the linear case,

12 November 2026 10:29:21

© Author(s) 2026

quantum-chemical calculations yield frequency-dependent molecular polarizability tensors, which are transformed into a T-matrix representation of the scatterer.[211] This representation is particularly powerful because it encodes the response of a molecular building block to arbitrary incident electromagnetic fields and can, therefore, be inserted naturally into multiple-scattering Maxwell solvers.[212,213] A T-matrix of a single scattering object, such as molecule or crystalline unit cell, can be efficiently arranged in a periodic lattice to calculate the total optical response of the multi-scattering system of the crystalline materials, thin films, and multi-layered multi-material designs. In this way, atomistic electronic-structure information is retained without requiring a prohibitively expensive quantum-chemical treatment of an entire nanostructure or molecular crystal. The hyper-T-matrix extends this idea to non-linear optics.[214,215] Instead of representing only the induced dipole response at the driving frequency, it maps quantum-chemically computed first hyperpolarizabilities, typically obtained from TDDFT or related response methods, onto the emitted second-harmonic field. This gives access to non-linear observables, such as second-harmonic or sum-frequency generation, while preserving the full tensorial, orientational, and dispersive character of the molecular response. The workflow is illustrated in Fig. 10.

A central strength of the method is that it treats the molecule not as a scalar effective susceptibility but as an optically active scattering object embedded in a realistic photonic environment. Taken together, the linear and hyper-T-matrix formalisms offer a practical multiscale route from electronic structure to device-level optics, often allowing for the targeted design optimization with desired optical response. They are especially valuable for molecular nanomaterials, chiral frameworks, thin films, and cavities, where local molecular properties, intermolecular electromagnetic coupling, and photonic resonances all influence the measured response.[216–221] Their main limitation is that the quality of the final prediction remains tied to the underlying quantum-chemical input and to how accurately the molecular environment is represented. Nevertheless, this approach is an important methodological advance because it avoids a strict separation between quantum chemistry and classical electrodynamics, enabling predictive simulations of complex linear and non-linear molecular photonic materials.

E. CCSDR(3) and CC3: Excitation energies with connected triples

A new feature introduced recently are electronic excitation energies with approximate coupled cluster methods that include connected triple excitations, namely, the iterative CC3 model[222,223] and the perturbative CCSDR(3) approximation.[223] Their efficient implementation in `ccsdf12` uses OpenMP parallelization and

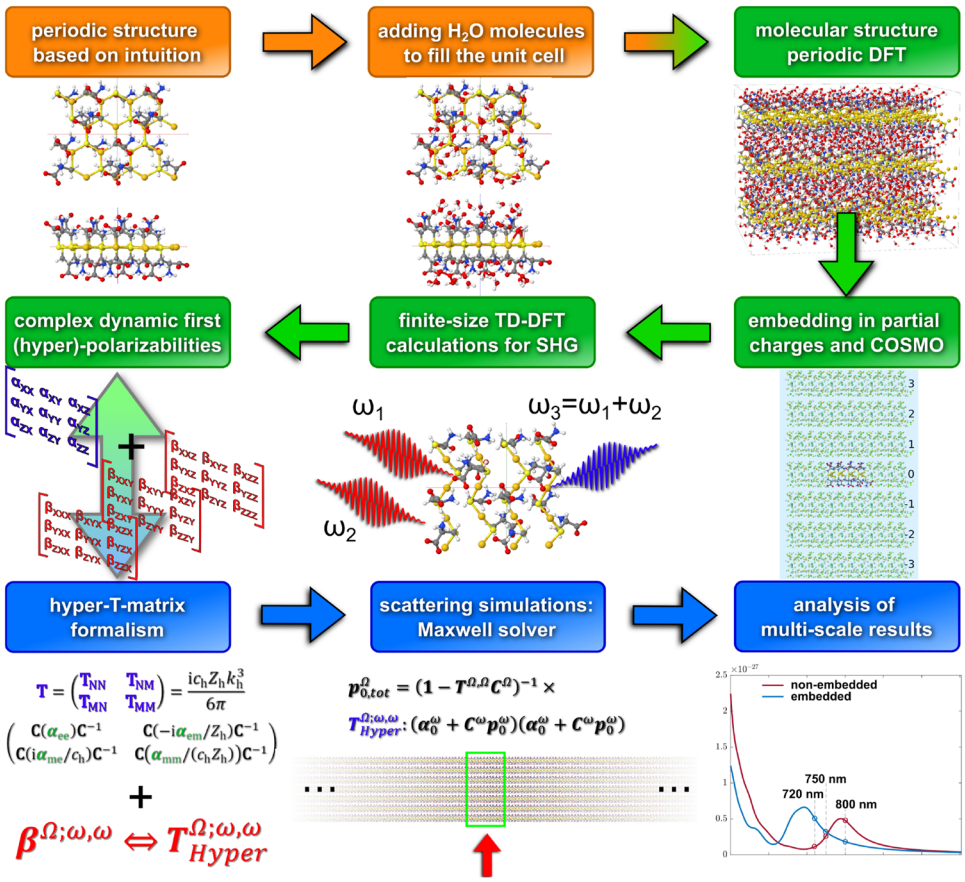


FIG. 10. A visual scheme for the multi-scale multi-scattering workflow combining quantum chemistry with scattering simulations for second harmonic generation of the supramolecular gold-cysteine self-assembled thin film dispersed in water. Reprinted with permission from Poleva *et al.*, J. Phys. Chem. C **129**, 17119 (2025). Copyright 2025 American Chemical Society.

12 November 2026 10:29:21

© Author(s) 2026

exploits molecular symmetry (D_{2h} and its subgroups). These third-order methods provide a significant extension by going beyond the previously available second-order methods CC2 and CCSD. For single-excitation dominated valence transitions, CC3 provides systematically better results (MSE: 0.008 eV) compared to both CC2 (MSE: 0.08 eV) and CCSD (MSE: 0.13 eV), based on mean signed errors (MSEs) with respect to CC4 (or higher levels) in the QUEST database.[224] Particularly, for this type of excitations, CCSD is generally less accurate than CC2. However, the improved accuracy of CC3 comes at drastically increased computational costs: CC3 scales as $\mathcal{O}(\mathcal{N}^7)$ with the system size $\mathcal{N}$, whereas CC2 and CCSD scale as $\mathcal{O}(\mathcal{N}^5)$ and $\mathcal{O}(\mathcal{N}^6)$, respectively. One possibility to tackle these heavy computational costs is to avoid the costly iterations in CC3 by calculating only a perturbative (non-iterative) triples correction to CCSD using CCSDR(3), reducing the costs to $\mathcal{O}(\mathcal{N}^6)$-scaling iterations and a non-iterative $\mathcal{O}(\mathcal{N}^7)$ step. Another possibility is to speed up the CC3 calculation itself by using a restricted virtual space (RVS), as suggested in Ref. 225.

Recently, we took advantage of the RVS approximation in a study on the solvatochromic dye 2,6-di-*tert*-butyl-4-pyridinium phenolate (**N1-tBu**),[226] shown in Fig. 11. A comparison of the first excitation energy (Table VIII) revealed a severe deviation between ADC(2) and CC2 of ~0.5 eV, rooted in a configuration mixing that is partially accounted for in CC2 through the ground-state singles amplitudes, but missing in ADC(2). In that study, CC3 provided evidence that CC2 is more accurate than ADC(2), which deviated in this case from CC3 by >0.4 eV, while CC2 agreed with CC3 within about 0.05 eV. The CC3 calculation took a wall time of ~8 days on a node with 2 × Intel Xeon(R) Gold 6430 (64 cores and 256 GB RAM in total), starting from CCSD and imposing C_{2v} symmetry. A significant speed-up was achieved by applying the RVS approximation (cutoff: $2E_H$), reducing the computing time by ~70% relative to the calculation in the full virtual space (FVS). At the CC3 level, the RVS approximation only introduced an insignificant error of 0.013 eV.

Moreover, the RVS approximation allows to construct a theoretical best estimate (TBE) for FVS-CC3 based on the RVS-CC3 result (2.242 eV) and the RVS error at the lower CC2 level (0.023 eV). This yields a TBE of 2.219 eV, which only differs by −0.010 eV from the FVS-CC3 result. In sharp contrast, the result with the perturbative triples correction appears less convincing. The CCSDR(3) result of 2.311 eV deviates from the CC3 value by 0.082 eV, which, in this case, is larger than the CC2–CC3 difference (0.040 eV). However, the CCSDR(3) calculation only takes ~20 h, i.e., ~10% of the time needed for the FVS or 35% of that for the RVS CC3 calculation.

TABLE VIII. First vertical excitation energies (VEEs) of **N1-tBu**. All excitation energies are given in eV.

Method	VEE($S_0 \rightarrow S_1$)		
	FVS	RVS	Error
ADC(2)	1.801	1.781	−0.020
CC2	2.269	2.292	+0.023
CC3	2.229	2.242	+0.013
TBE	2.229	2.219	−0.010
CCSDR(3)	2.311	⋯	⋯

VIII. EMBEDDING AND MULTISCALE FRAMEWORK

A. Consistent COSMO and GOSTSHYP

Solvation can be modeled with the continuum solvation model COSMO, which has been established for decades as a simple but reliable tool capable of capturing non-specific interactions between solute and solvent through electrostatic interactions on a molecular surface (cavity).[227] This can be done self-consistently within the SCF procedure by adding an additional energy contribution,[26]

$$E^{\mathrm{COSMO}} = -\frac{1}{2}\sum_{j=1}^{N_{\mathrm{seg}}} q_j \Phi_j, \tag{52}$$

where q_j is the COSMO charge on segment j, Φ_j is the respective potential on segment j produced by the electrons and nuclei of the solute, and the sum runs over all N_{seg} segments of the discretized cavity. Subsequent schemes can also model the linear response of this contribution, making it compatible with LR-TDDFT and the calculation of other response properties, including NMR shifts as well as geometry gradients and Hessians.[50,97,139,228] However, the choice of cavity and charge model are quite important for the consistency of the method. While many sophisticated schemes for the construction of the cavity, such as solvent-excluded surfaces and (pseudo-)isodensity surfaces, were implemented in TURBOMOLE already, none of them led to fully smooth potential energy surfaces and consistent derivatives.

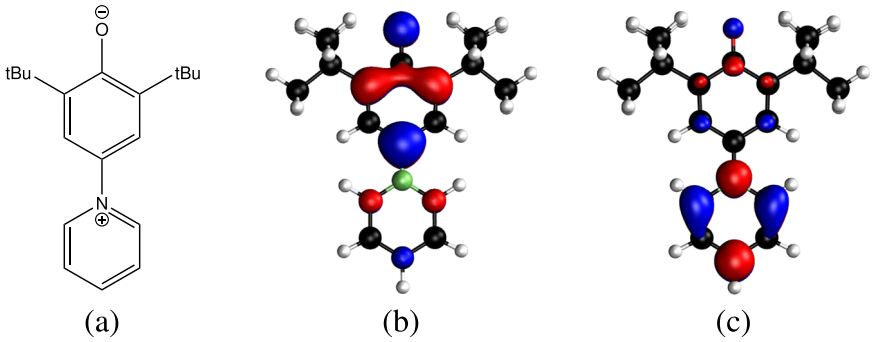


FIG. 11. Molecular structure (a) of **N1-tBu** and the occupied (b) and virtual (c) natural transition orbitals (NTOs) for the first electronic transition.

12 November 2026 10:29:21

© Author(s) 2026

We solved these problems by implementing a van-der-Waals surface based on hard spheres centered around the nuclei and replaced the point charges typically used in COSMO with a Gaussian charge model (GCM).[50,229] Since version 8.0, COSMO-GCM is the default model and it is implemented in all modules that support COSMO. It eliminates the artifacts in geometry optimization, transition state searches, and in the calculation of vibrational spectra, making all of these applications accessible.[50] However, it should be noted that COSMO-GCM is not yet compatible with COSMO-RS.

We further implemented the Gaussians On Surface Tesserae Simulate HYdrostatic Pressure (GOSTSHYP) model.[230–232] It is structurally very similar to COSMO but can be used to calculate mechanical pressure on the molecular and electronic structure instead. The GOSTSHYP energy contribution,[232]

$$E^{\mathrm{GOSTSHYP}} = \sum_{j=1}^{N_{\mathrm{seg}}} p_j \tilde{g}_j, \tag{53}$$

reflects the similarity to COSMO, requiring a self-consistent optimization of GOSTSHYP amplitudes p_j and overlaps $\tilde{g}_j$ instead. It is compatible with DFT and its geometry gradients, and we recently extended the framework to LR-TDDFT.[233] It can be used in combination with COSMO, leading to fairly accurate predictions of spectroscopic properties in the high pressure regime. We used a combined COSMO/GOSTSHYP approach to simulate the effects of high pressure on aromatic systems solved in methylcyclohexane, see Fig. 12.[233] In agreement with the experiment,[234] our model predicts red-shifts for the lowest electronic excitation of most aromatic compounds but an almost linear anomalous blue-shift for azulene. These calculations were performed with CAM-B3LYP-D4/def2-TZVPD.[235–237]

B. COSMO-CC2 with a fully self-consistent coupling scheme for absorption and emission spectra in solution

In our 2020 special issue contribution,[3] we reviewed the then new implementation of excitation energies, spectra, and ground- and excited-state gradients for CC2 and ADC(2) combined with the continuum solvation model COSMO and the atomistic polarizable embedding (PE) approach. This implementation employs a post-SCF reaction field coupling scheme, which introduces only minor computational overhead compared to gas-phase calculations. In addition to the ground-state reaction field, it includes linear-response (LR) contributions that account for the coupling of transition densities to the dynamic polarizability of the environment. These effects capture the dominant solvent influence on spectra when the initial state is the ground state.

Recently,[238] this approach has been extended to a perturbation-through-energy-and-density coupling scheme with LR contributions, denoted PTED(LR). In contrast to the post-SCF scheme, PTED(LR) employs a state-specific (SS) reaction field that is self-consistently equilibrated with the solute charge density for each initial state, including excited states. This treatment is essential for accurate potential energy surfaces of charge-transfer (CT) states and, thus, for emission spectra where CT states are involved, as well as for a balanced description of local and CT excitations.

A representative application are the absorption and emission spectra of protonated 5-methoxyquinoline in aqueous solution. This protonated photobase has two low-lying $\pi\pi^*$ states: $S_1(L_a)$ with partial CT character and $S_2(L_b)$ without significant charge transfer. For the spectra shown in Fig. 13, ground- and excited-state structures and harmonic vibrational frequencies were obtained at the PTED(LR)-COSMO-CC2/def2-TZVPP level. Electronic energies were refined using PTED(LR)-COSMO-CC2/def2-TZVPPD

12 November 2026 10:29:21

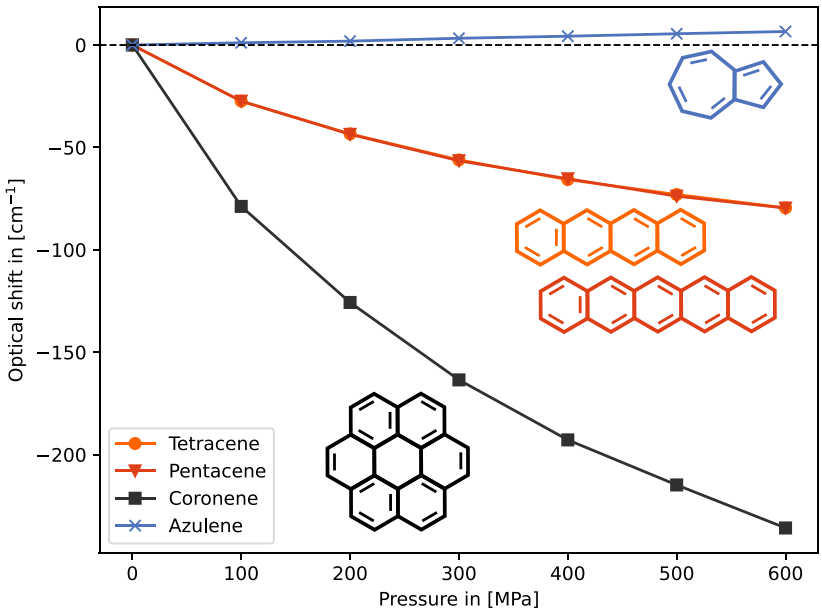


FIG. 12. Pressure-induced shifts of the lowest electronic excitation for various aromatic compounds calculated with LR-TDDFT COSMO/GOSTSHYP at the CAM-B3LYP-D4/def2-TZVPD level. In agreement with the experiment,[234] azulene exhibits an almost linear anomalous blue-shift. Plotted with computational data taken from Ref. 233.

© Author(s) 2026

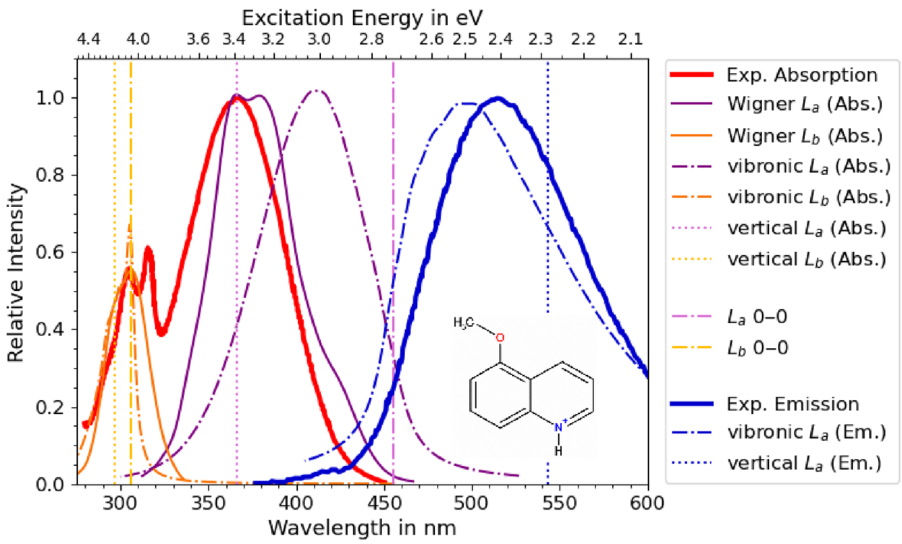


FIG. 13. 5-Methoxyquinolinium cation. Comparison of computed vibronic absorption and emission spectra and absorption spectra computed from a Wigner distribution with experimental spectra from Ref. 240 recorded in aqueous solution (digitized with WebPlotDigitizer[241]).

and further by adding the CC3–CC2 differences computed in the def2-TZVPP basis with the frozen PTED(LR)-COSMO-CC2/def2-TZVPP reaction fields included in the Hamiltonian. Vibronic absorption and emission spectra were then calculated using the harmonic frequencies. In addition, the absorption spectrum was calculated using the nuclear ensemble method[239] with a Wigner ensemble for the ground state and post-SCF-COSMO-CC2 excitation energies and oscillator strengths, with corrections for the transitions energies from the best estimates for the vertical transition energies.

This work flow reproduces for both states, L_a and L_b, within around 0.1 eV the experimental results for the 0–0 transition energies in aqueous solution, which are estimated for L_b from the band origin and for L_a from the intersection point between the absorption and emission bands. This accuracy could before only be reached for gas phase calculations. In addition, the bandwidths for L_b and L_a and the position of the band maximum for L_b are reproduced within about 0.1 eV. The position of the L_a band is reproduced with this accuracy only by the projection approach. The vibronic approach does within the harmonic approximation not reach this accuracy for the L_a absorption band, because of the large differences between the ground- and the L_a-state equilibrium structures.

C. Wavefunction methods embedded in DFT for periodic systems

Accurate prediction of adsorption energies is essential for elucidating surface interactions in heterogeneous catalysis, surface science, and materials science. DFT is widely employed for this purpose due to its favorable computational cost and ease of use. However, its performance is strongly dependent on the choice of exchange–correlation functional and can be unreliable in cases where dispersion and local correlation effects are not adequately captured. Even with semi-empirical dispersion corrections, such as Grimme's D3 correction,[68] significant errors may persist for weakly bound adsorption systems, motivating the use of correlated wavefunction methods. In this context, recent developments in periodic local correlation methods, in particular periodic DLPNO-MP2, are especially promising.[123–125] Alternatively, MP2-level adsorption energies can be obtained using a molecule-in-periodic embedding strategy based on the kinetic-energy-density functional (KEDF), denoted as `Method 2` in the documentation and implemented in the `riper` module, as demonstrated in Refs. 5 and 242–244.

Here, we employ this molecule-in-periodic embedding scheme to compute the adsorption energy of CO on the MgO(001) surface. The total system is described periodically at the DFT level, while a chemically relevant molecular cluster containing the adsorbed CO molecule and nearby MgO atoms is treated as the active subsystem at the MP2 level. Two active subsystems are considered, namely CO–Mg_5O_5 and CO–Mg_7O_7, to assess the convergence of the embedded adsorption energy with respect to the size of the correlated region. The remaining part of the periodic MgO slab acts as the environment and enters the active-subsystem calculation through a KEDF-based embedding potential.

The MP2-in-DFT adsorption energy is computed using the additive correction formula,

$$E_{\mathrm{ads}}^{\mathrm{MP2-in-DFT}} = E_{\mathrm{ads}}^{\mathrm{DFT}} + \left(E_{\mathrm{ads(emb)}}^{\mathrm{MP2}} - E_{\mathrm{ads(emb)}}^{\mathrm{DFT}}\right), \tag{54}$$

where

$$E_{\mathrm{ads(emb)}}^{\mathrm{MP2}} = E_{\mathrm{CO-Mg_xO_x(emb)}}^{\mathrm{MP2}} - E_{\mathrm{CO(isolated)}}^{\mathrm{MP2}} - E_{\mathrm{Mg_xO_x(emb)}}^{\mathrm{MP2}}, \tag{55}$$

and

$$E_{\mathrm{ads(emb)}}^{\mathrm{DFT}} = E_{\mathrm{CO-Mg_xO_x(emb)}}^{\mathrm{DFT}} - E_{\mathrm{CO(isolated)}}^{\mathrm{DFT}} - E_{\mathrm{Mg_xO_x(emb)}}^{\mathrm{DFT}}. \tag{56}$$

In Eq. (54), $E_{\mathrm{ads}}^{\mathrm{DFT}}$ is the adsorption energy of CO on the full periodic MgO(001) slab evaluated at the DFT level. The term in parentheses is a local correlation correction obtained from the embedded active subsystem. It measures how much the adsorption energy of the embedded molecular cluster changes when the active subsystem is treated at the MP2 level instead of the DFT level,

12 November 2026 10:29:21

© Author(s) 2026

while keeping the same embedding environment. Thus, the periodic DFT calculation provides the long-range electrostatic, polarization, and surface-environment contributions, whereas the embedded MP2 calculation corrects the local CO–MgO interaction region for wavefunction-level correlation effects.

The adsorption geometry and periodic surface model were taken from the recent periodic DLPNO-MP2 study of CO adsorption on MgO(001) by Tew and co-workers.[125] The model corresponds to the dilute coverage limit of 1/16 monolayer, with one CO molecule adsorbed on a two-layer MgO slab containing 16 Mg and 16 O atoms per layer. The total periodic system and the two active-subsystem choices used in the present embedding calculations are shown in Fig. 14.

Calculations were performed using the def2-TZVP basis set[43] and the universal auxiliary basis set.[246] The PBE exchange–correlation functional[42] was used for the periodic DFT calculation and for the DFT part of the embedding correction, while the Thomas–Fermi[247,248] KEDF was used for constructing the non-additive kinetic-energy contribution to the embedding potential. The periodic PBE adsorption energy was counterpoise corrected for basis-set superposition error.

The adsorption energies are summarized in Table IX. At the PBE level, the uncorrected adsorption energy is −19.3 kJ mol^{-1}. After counterpoise correction, this becomes −18.1 kJ mol^{-1}, corresponding to a DFT-level BSSE contribution of ∼1.2 kJ mol^{-1}. The MP2-in-DFT embedding correction increases the binding strength relative to PBE. For the smaller CO–Mg_5O_5 active subsystem, the MP2-in-DFT adsorption energy is −20.8 kJ mol^{-1}. Increasing the active subsystem to CO–Mg_7O_7 changes the adsorption energy only slightly, to −21.1 kJ mol^{-1}, demonstrating convergence with respect to the active-subsystem size.

After adding the relaxation contribution of +1.1 kJ mol^{-1} used in Ref. 125, the converged CO–Mg_7O_7 MP2-in-DFT adsorption energy becomes −20.0 kJ mol^{-1}. This is in excellent agreement with the periodic DLPNO-MP2 value of −20.0 ± 0.2 kJ mol^{-1}. The agreement is noteworthy because the computational cost of the present embedding calculation is only dominated by the periodic DFT calculation of the full CO/MgO system, which is used for the embedding potential construction. Once the embedding potential has been generated using `Method 2`, the subsequent molecular embedded MP2 calculations for the CO–Mg_5O_5 and CO–Mg_7O_7 active subsystems are comparatively inexpensive. Thus, for this weakly bound adsorption problem, the KEDF-based MP2-in-DFT approach recovers a periodic correlated-wavefunction-quality adsorption energy at a cost that is close to that of the underlying periodic DFT calculation.

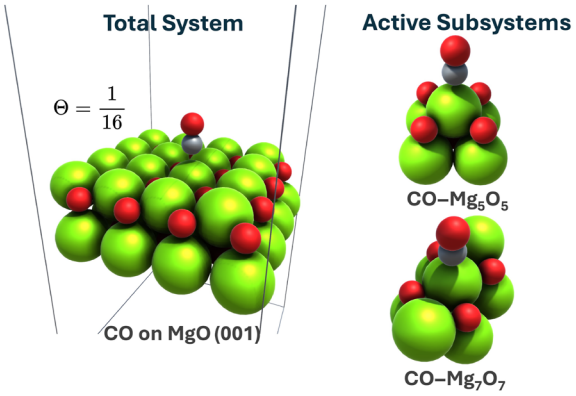


FIG. 14. Visualization of the periodic CO/MgO(001) adsorption model used in the embedded calculations. The left panel shows the full MgO(001) supercell with CO adsorbed at a surface coverage of Θ = 1/16. The right panels show the finite active subsystems, CO–Mg_5O_5 and CO–Mg_7O_7, selected from the periodic structure for the MP2-in-DFT embedding calculations. The molecular structures were rendered using the CrysX-3D Viewer.[245]

TABLE IX. Adsorption energy of CO on MgO(001) at dilute 1/16 surface coverage. All values are given in kJ mol^{-1}. The MP2-in-DFT values use the counterpoise-corrected PBE adsorption energy as the DFT reference term in Eq. (54). The last column adds the relaxation contribution of +1.1 kJ mol^{-1} used in Ref. 125 to facilitate direct comparison with the reported periodic DLPNO-MP2 adsorption energy.

Method	Active subsystem	E_{ads}	$E_{ads} + E_{relax}$
PBE, no CP correction	···	−19.3	−18.2
PBE, CP corrected	···	−18.1	−17.0
MP2-in-DFT	CO–Mg_5O_5	−20.8	−19.7
MP2-in-DFT	CO–Mg_7O_7	−21.1	−20.0
Periodic DLPNO-MP2[125]	···	···	−20.0 ± 0.2

D. Quantum computing for periodic systems through embedding

Quantum algorithms offer a promising route toward the simulation of electronic-structure problems whose computational cost increases rapidly with the number of electrons and orbitals. Among the algorithms proposed for near-term quantum devices, the variational quantum eigensolver (VQE) has attracted particular attention because it combines a parameterized quantum circuit with a classical optimization procedure.[249,250] VQE is, therefore, a hybrid quantum–classical algorithm.

Nevertheless, owing to the limitations of current quantum hardware, including the limited number and connectivity of qubits, imperfect quantum gates, and finite coherence times, the direct application of VQE to chemically realistic systems remains challenging.[250–252] In the literature, VQE calculations have largely been restricted to small molecules, such as TiH, LiH, NaH, and KH.[253] For larger molecules, VQE implementation has only been feasible after substantial reduction of the active orbital space.[254–256] These resource limitations become particularly restrictive for extended systems. Periodic VQE studies have, therefore, largely remained limited to small proof-of-principle models, including periodic hydrogen chains and simplified models of crystalline iron.[257,258] Treating an entire realistic periodic system at a correlated VQE level remains challenging with the capabilities of present-day quantum hardware and emulators.

This motivates the integration of VQE with quantum-embedding techniques. In the literature, VQE has been combined with projection-based embedding (PbE)[259,260] and density-matrix embedding theory (DMET).[261–263] We consider an alternative route using a KEDF-based embedding potential. The KEDF-based embedding is particularly advantageous for molecule-in-periodic embedding calculations, as it is reasonably accurate with a monomolecular basis.

12 November 2026 10:29:21

© Author(s) 2026

Here, we present preliminary results for a one-dimensional periodic LiH chain. A dedicated paper describing the implementation and its systematic validation is currently under preparation. It is now possible to generate and save the quantities required for a VQE calculation using TURBOMOLE. These quantities include the HF reference state and the one- and two-electron integrals required to construct the second-quantized fermionic Hamiltonian. These quantities can then be used to perform VQE using quantum computing libraries of one's choice, such as Qiskit[264] or PennyLane.[265] Here, we combine the PennyLane VQE solver with the KEDF-based molecule-in-periodic embedding and compute the cohesive energy of a 1D LiH chain using VQE-in-DFT.

To showcase the need for higher-level methods such as CCSD or VQE, we first compare the cohesive-energy curves of the LiH chain obtained using periodic DFT with the LDA and PBE functionals and periodic CCSD (Fig. 15). Both DFT approximations overbind relative to CCSD, with the overbinding being considerably larger for LDA. On the sampled 0.1 Å grid, all methods yield a minimum at $R = 1.7$ Å, although the minima are rather shallow. At this separation, the cohesive energies are −5.443, −4.878, and −4.398 eV/f.u. for LDA, PBE, and CCSD, respectively. Thus, relative to CCSD, LDA overbinds by ∼1.05 eV/f.u., while PBE reduces this error to ∼0.48 eV/f.u.

Since the VQE-in-DFT computations are performed using UCCSD *Ansatz* of the wavefunction, the embedded VQE results are expected to be in close agreement with the periodic CCSD calculations. The resulting cohesive-energy curve is shown in Fig. 15. The embedded VQE-in-DFT curve is in excellent agreement with the periodic CCSD calculation throughout the range of interatomic separations considered. At $R = 1.7$ Å, the cohesive energies obtained with VQE-in-DFT and periodic CCSD are −4.445 and −4.398 eV/f.u., respectively, corresponding to a difference of only ∼47 meV/f.u. This validates the implementation and demonstrates good accuracy compared to full periodic CCSD computation.

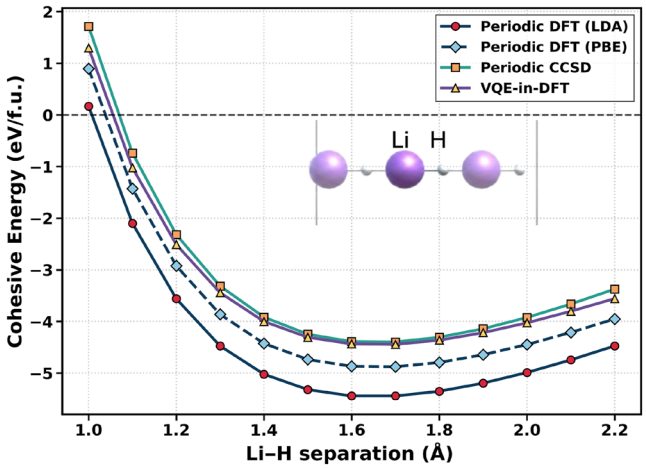


FIG. 15. Cohesive energy per LiH formula unit of the one-dimensional LiH chain as a function of the Li–H separation R. The fully periodic DFT (LDA and PBE) and CCSD curves are compared with the embedded VQE-in-DFT results. In the embedded calculations, the active subsystem is the central LiH formula unit, while the two neighboring LiH units form the DFT environment.

In addition, it is instructive to compare the formal scaling of VQE-in-DFT and CCSD-in-DFT embedding. For a UCCSD *Ansatz*, the number of variational amplitudes scales as $\mathcal{O}(N_{\mathrm{occ}}^2 N_{\mathrm{vir}}^2)$, whereas the dominant computational cost of conventional CCSD scales as $\mathcal{O}(N_{\mathrm{occ}}^2 N_{\mathrm{vir}}^4)$, where N_{occ} and N_{vir} denote the numbers of occupied and virtual orbitals, respectively. Thus, with comparable accuracy, VQE-in-DFT provides a more favorable scaling on quantum hardware than CCSD-in-DFT, although its practical cost also depends on circuit depth and measurement overhead.

Computational Details: The periodic reference curve for DFT (LDA/PBE) is obtained using TURBOMOLE, while that of CCSD is obtained with PySCF.[47] The computations are performed using the STO-3G basis set, where the primitive unit cell contains a single LiH formula unit. The Brillouin zone is sampled using eight k-points, which were found to be sufficient to converge the cohesive energy curve for the present benchmark.

For the embedded calculation, the periodic LiH chain is partitioned into an active molecular subsystem and a periodic environment. The total simulation cell contains three LiH formula units. The central LiH unit is considered as the active subsystem and treated using VQE, whereas the remaining two LiH units form the environment. The environment is described at the DFT LDA level, and the corresponding embedding potential is constructed using the KEDF-based molecule-in-periodic embedding scheme (`Method 2`). The VQE calculations reported here were performed using a classical quantum-circuit simulator rather than actual quantum hardware.

E. Real-time time dependent density functional embedding theory

Within real-time time dependent density functional embedding theory (RT-TDDFET), the system is partitioned into active (region of interest) and environment subsystems, and only the active subsystem's density is evolved in time, analogously to Eq. (48) via the density matrix $\mathbf{D}^{\mathbf{act}}(t)$ and the corresponding time-dependent KS matrix $\mathbf{F}^{\mathbf{act}}(t)$. The KS matrix of the active subsystem is augmented by an embedding contribution,

$$\mathbf{F}^{\mathrm{act}}(t) = \mathbf{F}^{\mathrm{KS}}[\mathbf{D}^{\mathrm{act}}(t)] + \mathbf{V}_{\mathrm{emb}}[\mathbf{D}^{\mathrm{act}}(t), \mathbf{D}^{\mathrm{env}}(t)], \tag{57}$$

where $\mathbf{V}_{\mathbf{emb}}$ is the DFT-based embedding potential matrix that depends on the densities (and in turn density matrices) of the active and environment subsystems. The embedding potential can be obtained either using KEDF-based or the level-shift projection operator (LSPO) technique.

In principle, both $\rho_{\mathrm{act}}(t)$ and $\rho_{\mathrm{env}}(t)$ can be propagated in time, allowing for a fully coupled dynamical treatment of subsystem polarization. However, a highly computationally efficient approximation is obtained by keeping the embedding potential fixed during the time evolution, i.e.,

$$\mathbf{V}_{\mathrm{emb}}(t) \approx \mathbf{V}_{\mathrm{emb}}[\mathbf{D}^{\mathrm{act}}(0), \mathbf{D}^{\mathrm{env}}(0)], \tag{58}$$

where the densities are taken from a prior ground-state or freeze-and-thaw calculation.

This "frozen-in-time" embedding approach avoids repeated evaluation of the embedding potential at each time step and thus provides drastic computational speedup, while still capturing the dominant environmental effects. It has been demonstrated to work

12 November 2026 10:29:21

© Author(s) 2026

really well for spectroscopic properties, such as absorption and high harmonic generation spectra, making RT-TDDFET a practical tool for large solvated or embedded systems.[5,242]

The KEDF-based RT-TDDFET implementation enables absorption spectra of solvated chromophores to be computed by propagating only the density of the active subsystem while retaining the dominant electrostatic and non-additive DFT contributions of the environment through a frozen embedding potential. As an illustrative example, we consider the lowest absorption band of methylenecyclopropene (MCP) solvated in water, using MCP as the active subsystem and the surrounding water molecules as the environment.

Two solvation models are used to demonstrate both molecular and periodic embedding capabilities. First, we employ a molecular MCP+$(H_2O)_{17}$ cluster geometry taken from a previous study and subsequently optimize it at the PBE-D3/def2-TZVP level. Second, we construct a periodic model consisting of one MCP molecule and 64 water molecules in a cubic cell of length 12.61 Å using RIPER Tools (web application for the `riper` related calculations),[5,266] followed by periodic geometry optimization at the PBE-D3 level of theory[42,68,267] and the pob-TZVP-rev2 basis set.[268]

For the subsequent embedding calculations, the PBE exchange–correlation functional[42] and the LC94 kinetic-energy density functional[269] are used to construct the embedding potential. The active MCP subsystem is described with the def2-TZVPD basis set[43,237] and the corresponding universal auxiliary basis set.[246] The absorption spectra of the isolated and embedded MCP molecule are then computed using RT-TDDFT and RT-TDDFET, respectively, with the SCAN0 hybrid meta-GGA functional.[270] The density is propagated for 2000 a.u. with a time step of 0.5 a.u. The KEDF-based embedding potential for RT-TDDFET is constructed using two choices of the environment density. In `Method 1`, the environment density is obtained from a molecular DFT calculation of the isolated environment. In `Method 2`, the environment density is approximated as $\tilde{\rho}^{\mathrm{env}} = \rho^{\mathrm{tot}} - \rho^{\mathrm{act}}_{\mathrm{iso}}$. Readers are referred to Refs. 242 and 243 and the official documentation for more details. In all RT-TDDFET simulations, the embedding potential is kept fixed during the real-time propagation.

Figure 16 compares the absorption spectra obtained for the two solvation models using the two embedding schemes. Note: For the periodic MCP+$(H_2O)_{64}$ model, only `Method 2` performs a proper molecule-in-periodic embedding with the water environment treated as periodic, whereas `Method 1` treats the water environment as a finite molecular cluster without periodic boundary conditions. For both solvation models, the isolated MCP molecule, computed using the corresponding solvated MCP geometry, shows the lowest excitation at 4.16 eV. For the molecular MCP+$(H_2O)_{17}$ cluster, the full-system LR-TDDFT calculation gives the lowest excitation at 4.84 eV. Both embedding schemes reproduce this blue shift quite well. `Method 1` yields the peak position of 4.84 eV, matching the full-system result exactly, and `Method 2` predicts the shifted peak at 4.76 eV. This agreement indicates that the frozen-environment RT-TDDFET is a useful tool to capture the solvent-induced shifts in the chromophore excitation energies, at a significantly reduced cost.

For the periodic MCP+$(H_2O)_{64}$ model, a direct full-system periodic LR-TDDFT reference is not available. Nevertheless, `Method 1` and the molecule-in-periodic `Method 2` calculation give approximately the same excitation energies, with the main absorption peak appearing at 4.65 and 4.70 eV, respectively. The similarity of the predicted shifts shows that the solvent effect is described consistently by the two embedding schemes, while the `Method 2` result demonstrates a molecule-in-periodic RT-TDDFET treatment that is difficult to access with conventional finite-system FDE implementations or full-system excited-state calculations.

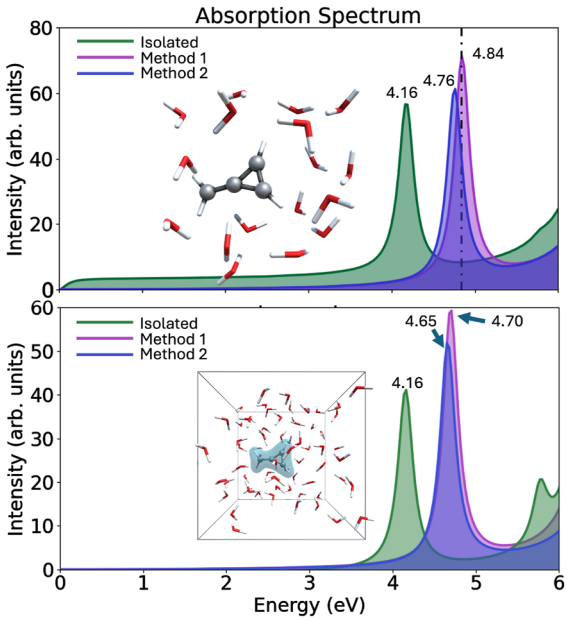


FIG. 16. RT-TDDFET absorption spectra of MCP solvated in water. (Top panel) Molecular MCP+$(H_2O)_{17}$ cluster. (Bottom panel) Periodic MCP+$(H_2O)_{64}$ model in a cubic water box. In both cases, the isolated MCP spectrum is computed using the solvated MCP geometry after removing the water environment. For MCP+$(H_2O)_{17}$, the vertical dashed line denotes the lowest excitation energy from the full-system LR-TDDFT calculation. For the periodic MCP+$(H_2O)_{64}$ model, no full-system periodic LR-TDDFT reference is available; the comparison, therefore, illustrates the consistency between the two KEDF-based embedding variants. The chemical structures are visualized using CrysX-3D Viewer.[245] The plots are generated using RIPER Tools.[5,266]

IX. SUMMARY AND OUTLOOK

During the last years, the capabilities of TURBOMOLE were expanded through systematic enhancements and the integration of new features. This makes TURBOMOLE a comprehensive and versatile tool for computational spectroscopy, mechanistic studies, and the *in silico* design of novel materials. New key features are the high methodological flexibility for the characterization of optical processes and magnetic properties as well as the consideration of environmental effects through embedding schemes or interfaces to third-party programs. Alongside these methodological improvements, the accessibility of the software suite was vastly improved with streamlined and short input formats relying on cutting-edge default settings and efficient parallelization to simplify and speed up computational workflows for both cost-efficient hardware and high-performance computing resources.

12 November 2026 10:29:21

© Author(s) 2026

As an outlook, the application of artificial-intelligence tools for software engineering recently accelerated the code development and maintenance. In particular, we expect that this benefits early-career developers by automating simple yet tedious tasks and aiding in the conceptual understanding and extension of the software suite.

Overall, TURBOMOLE has further transformed into a flexible toolbox with a focus on scientific rigor that also delivers user-friendliness, high performance, and extensive customization of workflows.

ACKNOWLEDGMENTS

The development of the program suite is organized by TURBOMOLE GmbH, a limited liability company located in Karlsruhe, Germany, which was founded in 2007. TURBOMOLE GmbH has adopted an irrevocable bylaw preventing the distribution of dividends to ensure that all profits are reinvested into the project. TURBOMOLE GmbH distributes fee-based end-user licenses itself and through partners, as well as free developer licenses and access to the source code based on project proposals. TURBOMOLE GmbH grants licenses for education and training free of charge. All past and present developers' contributions to the TURBOMOLE project are gratefully acknowledged. A list of contributors is available on the website.[271]

Y. J. Franzke was financially supported by TURBOMOLE GmbH and through the Walter–Benjamin program funded by the Deutsche Forschungsgemeinschaft (DFG, German Research Foundation)—Grant No. 518707327. M. Sharma gratefully acknowledges financial support from TURBOMOLE GmbH. F. Bruder and F. Weigend gratefully acknowledge support from the Deutsche Forschungsgemeinschaft (DFG, German Research Foundation) through the Collaborative Research Center "4f for Future" (CRC 1573 Project No. 471424360, project Q). P. Komonvasee gratefully acknowledges funding through the Institute for the Promotion of Teaching Science and Technology. A. Nejad was financially supported through the Walter–Benjamin program funded by the Deutsche Forschungsgemeinschaft (DFG, German Research Foundation)—Grant No. 517466522. A. Pausch gratefully acknowledges the support from the Walter–Benjamin program funded by DFG under Grant No. DFG-529675149 and financial support by Fonds der Chemischen Industrie (FCI) via a Liebig fellowship. M. Krstić gratefully acknowledges funding by the Volkswagen Foundation. R. Zielke thanks TURBOMOLE GmbH for financial support. M. Sierka gratefully acknowledges financial support from DFG within the Collaborative Research Center "NOA—Nonlinear Optics down to Atomic scales" (CRC 1375 Project No. 398816777, subproject A4) and the Research Training Group "PhInt—Photo-Polarizable Interfaces and Membranes" (GRK 3014, Project No. 521747072), the Carl Zeiss Foundation within the Breakthrough Program, and TURBOMOLE GmbH. N. Sülzner and C. Hättig thank the Deutsche Forschungsgemeinschaft (DFG, German Research Foundation) for funding through Project No. 388390466 (Grant No. CRC/TRR 247) and under Germany's Excellence Strategy—Grant No. Exc 2033—390677874—RESOLV.

AUTHOR DECLARATIONS

Conflict of Interest

Christof Hättig, Christof Holzer, and David P. Tew have an equity interest in TURBOMOLE GmbH. Marek Sierka and Florian Weigend have an equity interest in TURBOMOLE GmbH and serve as its chief executive officers. Uwe Huniar is an employee of Dassault Systèmes Deutschland GmbH, which commercially distributes the TURBOMOLE quantum chemistry software suite.

Author Contributions

Y. J. Franzke. and M. Sharma contributed equally to this work.

Yannick J. Franzke: Conceptualization (lead); Data curation (equal); Formal analysis (equal); Investigation (equal); Methodology (equal); Software (lead); Visualization (equal); Writing – original draft (lead); Writing – review & editing (lead). **Manas Sharma**: Conceptualization (lead); Data curation (equal); Formal analysis (equal); Investigation (equal); Methodology (equal); Software (lead); Visualization (equal); Writing – original draft (lead); Writing – review & editing (lead). **Priyanshi Bhasin**: Conceptualization (supporting); Data curation (equal); Formal analysis (equal); Investigation (equal); Methodology (equal); Visualization (equal); Writing – original draft (equal); Writing – review & editing (supporting). **Florian Bruder**: Conceptualization (supporting); Data curation (equal); Formal analysis (equal); Investigation (equal); Methodology (equal); Software (equal); Visualization (equal); Writing – review & editing (supporting). **Uwe Huniar**: Conceptualization (lead); Formal analysis (equal); Investigation (equal); Software (equal); Writing – original draft (equal); Writing – review & editing (equal). **Poramas Komonvasee**: Conceptualization (supporting); Data curation (equal); Formal analysis (equal); Investigation (equal); Methodology (equal); Software (equal); Visualization (equal); Writing – review & editing (supporting). **Marjan Krstić**: Conceptualization (supporting); Data curation (equal); Formal analysis (equal); Investigation (equal); Methodology (equal); Visualization (equal); Writing – review & editing (supporting). **Arman Nejad**: Conceptualization (supporting); Data curation (equal); Formal analysis (equal); Investigation (equal); Methodology (equal); Software (equal); Visualization (equal); Writing – review & editing (supporting). **Amber Pausch**: Conceptualization (supporting); Data curation (equal); Formal analysis (equal); Investigation (equal); Methodology (equal); Software (equal); Visualization (equal); Writing – original draft (equal); Writing – review & editing (equal). **Kesha Sorathia**: Conceptualization (supporting); Data curation (equal); Formal analysis (equal); Investigation (equal); Methodology (equal); Software (equal); Visualization (equal); Writing – review & editing (supporting). **Niklas Sülzner**: Conceptualization (supporting); Data curation (equal); Formal analysis (equal); Investigation (equal); Methodology (equal); Software (supporting); Visualization (equal); Writing – original draft (equal); Writing – review & editing (equal). **Ömer Faruk Can Tiska**: Conceptualization (supporting); Data curation (supporting); Formal analysis (supporting); Investigation

12 November 2026 10:29:21

© Author(s) 2026

(equal); Writing – review & editing (supporting). **Andrew Zhu**: Conceptualization (supporting); Data curation (equal); Formal analysis (equal); Investigation (equal); Methodology (equal); Software (equal); Visualization (equal); Writing – review & editing (supporting). **Roman Zielke**: Conceptualization (supporting); Data curation (equal); Formal analysis (equal); Investigation (equal); Methodology (equal); Software (equal); Visualization (equal); Writing – original draft (equal); Writing – review & editing (equal). **Christof Hättig**: Conceptualization (lead); Data curation (equal); Formal analysis (equal); Investigation (equal); Methodology (equal); Software (lead); Visualization (equal); Writing – original draft (equal); Writing – review & editing (equal). **Christof Holzer**: Conceptualization (lead); Data curation (equal); Formal analysis (equal); Investigation (equal); Methodology (equal); Software (lead); Writing – original draft (lead); Writing – review & editing (equal). **Marek Sierka**: Conceptualization (lead); Data curation (equal); Formal analysis (equal); Investigation (equal); Methodology (equal); Software (lead); Writing – original draft (equal); Writing – review & editing (equal). **David P. Tew**: Conceptualization (lead); Data curation (equal); Formal analysis (equal); Investigation (equal); Methodology (equal); Software (lead); Writing – original draft (equal); Writing – review & editing (equal). **Florian Weigend**: Conceptualization (lead); Data curation (equal); Formal analysis (equal); Investigation (equal); Methodology (equal); Software (supporting); Writing – original draft (equal); Writing – review & editing (equal).

DATA AVAILABILITY

Most data that support the findings of this study are available within the article and the original references for the results. The benchmark data underlying the comparison of the new geometry optimizer are openly available on Zenodo, namely the 1752-molecule GFN2-xTB minimization set at https://doi.org/10.5281/zenodo.20395324 (Ref. 76) and the RGD1-TSopt-GFN2 transition-state set at https://doi.org/10.5281/zenodo.20489311 (Ref. 79). Further data are available from the corresponding authors upon reasonable request. TURBOMOLE is available from the webpage https://www.turbomole.org/ as compiled binaries. The program suite can be obtained free of charge for students and educational purposes.

REFERENCES

[1] R. Ahlrichs, M. Bär, M. Häser, H. Horn, and C. Kölmel, Chem. Phys. Lett. **162**, 165 (1989).
[2] F. Furche, R. Ahlrichs, C. Hättig, W. Klopper, M. Sierka, and F. Weigend, Wiley Interdiscip. Rev.: Comput. Mol. Sci. **4**, 91 (2014).
[3] S. G. Balasubramani, G. P. Chen, S. Coriani, M. Diedenhofen, M. S. Frank, Y. J. Franzke, F. Furche, R. Grotjahn, M. E. Harding, C. Hättig, A. Hellweg, B. Helmich-Paris, C. Holzer, U. Huniar, M. Kaupp, A. Marefat Khah, S. Karbalaei Khani, T. Müller, F. Mack, B. D. Nguyen, S. M. Parker, E. Perlt, D. Rappoport, K. Reiter, S. Roy, M. Rückert, G. Schmitz, M. Sierka, E. Tapavicza, D. P. Tew, C. van Wüllen, V. K. Voora, F. Weigend, A. Wodyński, and J. M. Yu, J. Chem. Phys. **152**, 184107 (2020).
[4] Y. J. Franzke, C. Holzer, J. H. Andersen, T. Begušić, F. Bruder, S. Coriani, F. Della Sala, E. Fabiano, D. A. Fedotov, S. Fürst, S. Gillhuber, R. Grotjahn, M. Kaupp, M. Kehry, M. Krstić, F. Mack, S. Majumdar, B. D. Nguyen, S. M. Parker, F. Pauly, A. Pausch, E. Perlt, G. S. Phun, A. Rajabi, D. Rappoport, B. Samal, T. Schrader, M. Sharma, E. Tapavicza, R. S. Treß, V. Voora, A. Wodyński, J. M. Yu, B. Zerulla, F. Furche, C. Hättig, M. Sierka, D. P. Tew, and F. Weigend, J. Chem. Theory Comput. **19**, 6859 (2023).
[5] M. Sharma, Y. J. Franzke, C. Holzer, F. Pauly, and M. Sierka, J. Phys. Chem. A **129**, 9062 (2025).
[6] C. D. Sherrill, D. E. Manolopoulos, T. J. Martínez, and A. Michaelides, J. Chem. Phys. **153**, 070401 (2020).
[7] J. E. Bates and F. Furche, J. Chem. Phys. **137**, 164105 (2012).
[8] T. M. Maier, A. V. Arbuznikov, and M. Kaupp, Wiley Interdiscip. Rev.: Comput. Mol. Sci. **9**, e1378 (2018).
[9] C. Holzer, J. Chem. Phys. **153**, 184115 (2020).
[10] C. Holzer, Y. J. Franzke, and M. Kehry, J. Chem. Theory Comput. **17**, 2928 (2021).
[11] H. Eshuis, J. Yarkony, and F. Furche, J. Chem. Phys. **132**, 234114 (2010).
[12] A. M. Burow, J. E. Bates, F. Furche, and H. Eshuis, J. Chem. Theory Comput. **10**, 180 (2014).
[13] K. Krause and W. Klopper, J. Comput. Chem. **38**, 383 (2017).
[14] X. Gui, C. Holzer, and W. Klopper, J. Chem. Theory Comput. **14**, 2127 (2018).
[15] C. Holzer and W. Klopper, J. Chem. Phys. **150**, 204116 (2019).
[16] C. Hättig and F. Weigend, J. Chem. Phys. **113**, 5154 (2000).
[17] C. Hättig, A. Hellweg, and A. Köhn, Phys. Chem. Chem. Phys. **8**, 1159 (2006).
[18] G. Schmitz and C. Hättig, J. Chem. Phys. **145**, 234107 (2016).
[19] G. Schmitz and C. Hättig, J. Chem. Theory Comput. **13**, 2623 (2017).
[20] M. S. Frank, G. Schmitz, and C. Hättig, Mol. Phys. **115**, 343 (2017).
[21] D. P. Tew, J. Chem. Theory Comput. **15**, 6597 (2019).
[22] M. K. Armbruster, F. Weigend, C. van Wüllen, and W. Klopper, Phys. Chem. Chem. Phys. **10**, 1748 (2008).
[23] A. Baldes and F. Weigend, Mol. Phys. **111**, 2617 (2013).
[24] D. Peng, N. Middendorf, F. Weigend, and M. Reiher, J. Chem. Phys. **138**, 184105 (2013).
[25] Y. J. Franzke, N. Middendorf, and F. Weigend, J. Chem. Phys. **148**, 104110 (2018).
[26] A. Schäfer, A. Klamt, D. Sattel, J. C. W. Lohrenz, and F. Eckert, Phys. Chem. Chem. Phys. **2**, 2187 (2000).
[27] A. Klamt, Wiley Interdiscip. Rev.: Comput. Mol. Sci. **1**, 699 (2011).
[28] A. Klamt and M. Diedenhofen, J. Phys. Chem. A **119**, 5439 (2015).
[29] A. Hellweg and F. Eckert, AIChE J. **63**, 3944 (2017).
[30] K. Eichkorn, O. Treutler, H. Öhm, M. Häser, and R. Ahlrichs, Chem. Phys. Lett. **242**, 652 (1995).
[31] M. Sierka, A. Hogekamp, and R. Ahlrichs, J. Chem. Phys. **118**, 9136 (2003).
[32] F. Weigend, Phys. Chem. Chem. Phys. **4**, 4285 (2002).
[33] F. Weigend and M. Häser, Theor. Chem. Acc. **97**, 331 (1997).
[34] F. Weigend, M. Kattannek, and R. Ahlrichs, J. Chem. Phys. **130**, 164106 (2009).
[35] A. M. Burow, M. Sierka, and F. Mohamed, J. Chem. Phys. **131**, 214101 (2009).
[36] R. Łazarski, A. M. Burow, and M. Sierka, J. Chem. Theory Comput. **11**, 3029 (2015).
[37] R. Łazarski, A. M. Burow, L. Grajciar, and M. Sierka, J. Comput. Chem. **37**, 2518 (2016).
[38] C. Steffen, K. Thomas, U. Huniar, A. Hellweg, O. Rubner, and A. Schroer, J. Comput. Chem. **31**, 2967 (2010).
[39] BASF SE and Matgenix SRL, Turbomoleio, a python library containing a set of tools for the generation of inputs and parsing of outputs for TURBOMOLE, current version 1.6.0, https://github.com/Matgenix/turbomoleio (retrieved 22 March 2026).
[40] See https://github.com/grimme-lab/cefine for Grimme lab github site (retrieved 22 May 2026).
[41] A. H. Larsen, J. J. Mortensen, J. Blomqvist, I. E. Castelli, R. Christensen, M. Dułak, J. Friis, M. N. Groves, B. Hammer, C. Hargus, E. D. Hermes, P. C. Jennings, P. B. Jensen, J. Kermode, J. R. Kitchin, E. L. Kolsbjerg, J. Kubal, K. Kaasbjerg, S. Lysgaard, J. B. Maronsson, T. Maxson, T. Olsen, L. Pastewka, A. Peterson, C. Rostgaard, J. Schiøtz, O. Schütt, M. Strange, K. S. Thygesen, T. Vegge, L. Vilhelmsen, M. Walter, Z. Zeng, and K. W. Jacobsen, J. Phys.: Condens. Matter **29**, 273002 (2017).
[42] J. P. Perdew, K. Burke, and M. Ernzerhof, Phys. Rev. Lett. **77**, 3865 (1996).

12 November 2026 10:29:21

© Author(s) 2026

[43]F. Weigend and R. Ahlrichs, Phys. Chem. Chem. Phys. **7**, 3297 (2005).
[44]E. Caldeweyher, S. Ehlert, A. Hansen, H. Neugebauer, S. Spicher, C. Bannwarth, and S. Grimme, J. Chem. Phys. **150**, 154122 (2019).
[45]Y. Zhao and D. G. Truhlar, Theor. Chem. Acc. **120**, 215 (2008).
[46]F. Ju, X. Wei, L. Huang, A. J. Jenkins, L. Xia, J. Zhang, J. Zhu, H. Yang, B. Shao, P. Dai, D. B. Williams-Young, A. Mayya, Z. Hooshmand, A. Efimovskaya, N. A. Baker, M. Troyer, and H. Liu, J. Chem. Theory Comput. **20**, 10838 (2024).
[47]Q. Sun, X. Zhang, S. Banerjee, P. Bao, M. Barbry, N. S. Blunt, N. A. Bogdanov, G. H. Booth, J. Chen, Z.-H. Cui, J. J. Eriksen, Y. Gao, S. Guo, J. Hermann, M. R. Hermes, K. Koh, P. Koval, S. Lehtola, Z. Li, J. Liu, N. Mardirossian, J. D. McClain, M. Motta, B. Mussard, H. Q. Pham, A. Pulkin, W. Purwanto, P. J. Robinson, E. Ronca, E. R. Sayfutyarova, M. Scheurer, H. F. Schurkus, J. E. T. Smith, C. Sun, S.-N. Sun, S. Upadhyay, L. K. Wagner, X. Wang, A. White, J. D. Whitfield, M. J. Williamson, S. Wouters, J. Yang, J. M. Yu, T. Zhu, T. C. Berkelbach, S. Sharma, A. Y. Sokolov, and G. K.-L. Chan, J. Chem. Phys. **153**, 024109 (2020).
[48]TURBOMOLE GmbH, TURBOMOLE V7.7 2023, a development of University of Karlsruhe and Forschungszentrum Karlsruhe GmbH, 1989-2007, TURBOMOLE GmbH, since 2007, available from https://www.turbomole.org, 2023 (retrieved 5 May 2026).
[49]A. Schäfer, H. Horn, and R. Ahlrichs, J. Chem. Phys. **97**, 2571 (1992).
[50]A. Pausch, J. Chem. Theory Comput. **20**, 3169 (2024).
[51]O. Treutler and R. Ahlrichs, J. Chem. Phys. **102**, 346 (1995).
[52]S. Lehtola, J. Chem. Theory Comput. **15**, 1593 (2019).
[53]TURBOMOLE GmbH, Manual of TURBOMOLE V8.0 2025, a development of University of Karlsruhe and Forschungszentrum Karlsruhe GmbH, 1989-2007, TURBOMOLE GmbH, since 2007, available from https://www.turbomole.org/turbomole/turbomole-documentation/, 2025 (retrieved 5 May 2026).
[54]TURBOMOLE GmbH, TURBOMOLE online manual, https://manual.turbomole.org (retrieved 26 June 2026)
[55]See https://github.com/microsoft/accelerated-dft/tree/main/benchmarks for Microsoft Accelerated DFT (accessed 22 May, 2026).
[56]R. Bauernschmitt and R. Ahlrichs, J. Chem. Phys. **104**, 9047 (1996).
[57]The examples rev_xx11118 and rev_xx11193 need more than 100 SCF iterations to converge for the closed shell case, but they both converge to −7.7 and −2.7 kcal/mol lower energies than reported. For the oxygen atom, also part of the benchmark set, TURBOMOLE has chosen the more stable triplet state by default, leading to a −59.7 kcal/mol lower total energy. The triplet energies of rev_xx11118 and rev_xx11193 are −44.1 and −45.1 kcal/mol lower than the reported instable singlet case. FeBF4 is the most interesting case, as the closed shell energy is −79.5 kcal/mol lower than reported by Accelerated DFT and PySCF for unknown reasons.
[58]M. Häser, J. Chem. Phys. **95**, 8259 (1991).
[59]M. Häser, J. Almlöf, and M. W. Feyereisen, Theor. Chem. Acc. **79**, 115 (1991).
[60]H. Weiss, R. Ahlrichs, and M. Häser, J. Chem. Phys. **99**, 1262 (1993).
[61]C. van Wüllen, Chem. Phys. Lett. **219**, 8 (1994).
[62]F. Haase and R. Ahlrichs, J. Comput. Chem. **14**, 907 (1993).
[63]F. Mack, C. J. Schattenberg, M. Kaupp, and F. Weigend, J. Phys. Chem. A **124**, 8529 (2020).
[64]M. Kollwitz, M. Häser, and J. Gauss, J. Chem. Phys. **108**, 8295 (1998).
[65]R. Lindh, A. Bernhardsson, G. Karlström, and P.-Å. Malmqvist, Chem. Phys. Lett. **241**, 423 (1995).
[66]R. Fletcher, *Practical Methods of Optimization*, 2nd ed. (Wiley, Chichester, 1987).
[67]P. Pyykkö and M. Atsumi, Chem. Eur. J. **15**, 186 (2009).
[68]S. Grimme, J. Antony, S. Ehrlich, and H. Krieg, J. Chem. Phys. **132**, 154104 (2010).
[69]J. Baker, J. Comput. Chem. **14**, 1085 (1993).
[70]L. Goerigk, A. Hansen, C. Bauer, S. Ehrlich, A. Najibi, and S. Grimme, Phys. Chem. Chem. Phys. **19**, 32184 (2017).
[71]D. Balcells and B. B. Skjelstad, J. Chem. Inf. Model. **60**, 6135 (2020).
[72]A. B. Birkholz and H. B. Schlegel, Theor. Chem. Acc. **135**, 84 (2016).
[73]C. Bannwarth, S. Ehlert, and S. Grimme, J. Chem. Theory Comput. **15**, 1652 (2019).
[74]L.-P. Wang and C. Song, J. Chem. Phys. **144**, 214108 (2016).
[75]C. Bannwarth, E. Caldeweyher, S. Ehlert, A. Hansen, P. Pracht, J. Seibert, S. Spicher, and S. Grimme, Wiley Interdiscip. Rev.: Comput. Mol. Sci. **11**, e1493 (2021).
[76]M. Sierka (2026). "A 1752-molecule benchmark set for molecular geometry optimizers on the GFN2-xTB potential energy surface," Zenodo. https://doi.org/10.5281/zenodo.20395324
[77]A. Banerjee, N. Adams, J. Simons, and R. Shepard, J. Phys. Chem. **89**, 52 (1985).
[78]J. Baker, J. Comput. Chem. **7**, 385 (1986).
[79]M. Sierka (2026). "RGD1-TSopt-GFN2: A transition-state optimization benchmark on the GFN2-xTB surface," Zenodo. https://doi.org/10.5281/zenodo.20489311
[80]Q. Zhao, S. M. Vaddadi, M. Woulfe, L. A. Ogunfowora, S. S. Garimella, O. Isayev, and B. M. Savoie, Sci. Data **10**, 145 (2023).
[81]J. Jaramillo, G. E. Scuseria, and M. Ernzerhof, J. Chem. Phys. **118**, 1068 (2003).
[82]C. Holzer and Y. J. Franzke, J. Chem. Theory Comput. **21**, 202 (2025).
[83]C. Holzer and Y. J. Franzke, ChemPhysChem **25**, e202400120 (2024).
[84]L. Steffen, L. S. Szych, Y. J. Franzke, R. O. Kopp, M. J. Ernst, M. Weber, and C. Müller, Chem. Commun. **61**, 14907 (2025).
[85]C. Kruck, T. Neumann, A. Schäfer, E. Kreidt, P. Weis, C. Holzer, M. M. Kappes, and M. Seitz, Inorg. Chem. **64**, 22048 (2025).
[86]V. N. Rai, C. Holzer, C. Rockstuhl, W. Wulfhekel, and L. Gerhard, ACS Nano **20**, 12173 (2026).
[87]F. Wiedemaier, D. M. Köpfler, C. Schlegl, C. Holzer, F. Belaj, N. C. Mösch-Zanetti, and J. A. Schachner, J. Catal. **453**, 116526 (2026).
[88]F. Pavošević, T. Culpritt, and S. Hammes-Schiffer, Chem. Rev. **120**, 4222 (2020).
[89]S. Hammes-Schiffer, J. Chem. Phys. **155**, 030901 (2021).
[90]R. E. Warburton, A. V. Soudackov, and S. Hammes-Schiffer, Chem. Rev. **122**, 10599 (2022).
[91]J. Vohdin and C. Holzer, J. Chem. Phys. **165**, 124109 (2026).
[92]J. F. Dobson, J. Chem. Phys. **98**, 8870 (1993).
[93]J. Tao, Phys. Rev. B **71**, 205107 (2005).
[94]A. D. Becke, J. Chem. Phys. **117**, 6935 (2002).
[95]C. J. Schattenberg and M. Kaupp, J. Chem. Theory Comput. **17**, 1469 (2021).
[96]Y. J. Franzke and C. Holzer, J. Chem. Phys. **157**, 031102 (2022).
[97]F. Bruder, Y. J. Franzke, and F. Weigend, J. Phys. Chem. A **126**, 5050 (2022).
[98]F. Bruder, Y. J. Franzke, C. Holzer, and F. Weigend, J. Chem. Phys. **159**, 194117 (2023).
[99]R. Grotjahn and F. Furche, J. Chem. Theory Comput. **19**, 4897 (2023).
[100]J. Sun, A. Ruzsinszky, and J. P. Perdew, Phys. Rev. Lett. **115**, 036402 (2015).
[101]J. Tao, J. P. Perdew, V. N. Staroverov, and G. E. Scuseria, Phys. Rev. Lett. **91**, 146401 (2003).
[102]J. W. Furness, J. Verbeke, E. I. Tellgren, S. Stopkowicz, U. Ekström, T. Helgaker, and A. M. Teale, J. Chem. Theory Comput. **11**, 4169 (2015).
[103]T. J. P. Irons, G. David, and A. M. Teale, J. Chem. Theory Comput. **17**, 2166 (2021).
[104]T. Saue, ChemPhysChem **12**, 3077 (2011).
[105]A. Pausch and C. Holzer, J. Phys. Chem. Lett. **13**, 4335 (2022).
[106]C. Holzer, Y. J. Franzke, and A. Pausch, J. Chem. Phys. **157**, 204102 (2022).
[107]Y. J. Franzke and C. Holzer, J. Chem. Phys. **160**, 184101 (2024).
[108]Y. J. Franzke, A. Pausch, and C. Holzer, J. Chem. Phys. **162**, 084104 (2025).
[109]C. Hättig, D. P. Tew, and A. Köhn, J. Chem. Phys. **132**, 231102 (2010).
[110]D. P. Tew and W. Klopper, Mol. Phys. **108**, 315 (2010).
[111]D. P. Tew, J. Chem. Phys. **145**, 074103 (2016).
[112]D. P. Tew and C. Hättig, Int. J. Quantum Chem. **113**, 224 (2013).
[113]G. Schmitz, C. Hättig, and D. P. Tew, Phys. Chem. Chem. Phys. **16**, 22167 (2014).
[114]D. P. Tew, *New Electron Correlation Methods and Their Applications, and Use of Atomic Orbitals with Exponential Asymptotes*, *Advances in Quantum Chemistry Vol. 83*, edited by M. Musial and P. E. Hoggan (Academic Press, 2021), pp. 83–106.
[115]M. Schwilk, D. Usvyat, and H.-J. Werner, J. Chem. Phys. **142**, 121102 (2015).
[116]K. Sorathia and D. P. Tew, J. Chem. Phys. **153**, 174112 (2020).

12 November 2026 10:29:21

© Author(s) 2026

[117]K. Sorathia, D. Frantzov, and D. P. Tew, J. Chem. Theory Comput. **20**, 2740 (2024).
[118]V. Austen, T. Yanai, and Q. M. Phung, Inorg. Chem. **65**, 11853 (2026).
[119]L. R. Maurer, M. Bursch, S. Grimme, and A. Hansen, J. Chem. Theory Comput. **17**, 6134 (2021).
[120]A. Irmler, A. M. Burow, and F. Pauly, J. Chem. Theory Comput. **14**, 4567 (2018).
[121]G. Knizia, J. Chem. Theory Comput. **9**, 4834 (2013).
[122]A. Zhu and D. P. Tew, J. Phys. Chem. A **128**, 8570 (2024).
[123]A. Nejad, A. Zhu, K. Sorathia, and D. P. Tew, J. Chem. Phys. **163**, 214107 (2025).
[124]A. Zhu, A. Nejad, P. Komonvasee, K. Sorathia, and D. P. Tew, J. Chem. Phys. **163**, 214108 (2025).
[125]A. Zhu, P. Komonvasee, A. Nejad, and D. P. Tew, J. Chem. Theory Comput. **22**, 3927 (2026).
[126]R. Zielke, F. Weigend, and C. Holzer, Phys. Chem. Chem. Phys. **27**, 12284 (2025).
[127]W. Zou, M. Filatov, and D. Cremer, J. Chem. Phys. **142**, 214106 (2015).
[128]J. C. Boettger, Phys. Rev. B **62**, 7809 (2000).
[129]J. Ehrman, E. Martinez-Baez, A. J. Jenkins, and X. Li, J. Chem. Theory Comput. **19**, 5785 (2023).
[130]A. Kramida, Y. Ralchenko, J. Reader, and NIST ASD Team, NIST Atomic Spectra Database (ver. 5.12), National Institute of Standards and Technology, Gaithersburg, MD, 2024, available: https://physics.nist.gov/asd.
[131]S. Baweja, M. M. Kappes, A. Schäfer, A. Znotins, R. Zielke, C. Holzer, T. Neumann, C. Kruck, and M. Seitz, J. Phys. Chem. Lett. **16**, 13046 (2025).
[132]L. M. Mottram, Y. Chen, P. W. Smith, S. Klyatskaya, A. Ghiami, S. Schuppler, P. Nagel, H. Ramanantoanina, S. G. Minasian, D. Guenzing, A. T. N'Diaye, C. Holzer, M. Ruben, and B. Schacherl, chemRxiv:10.26434/chemrxiv.15000965/v1 (2026).
[133]K. Reiter, F. Mack, and F. Weigend, J. Chem. Theory Comput. **14**, 191 (2018).
[134]K. Reiter, M. Kühn, and F. Weigend, J. Chem. Phys. **146**, 054102 (2017).
[135]Y. J. Franzke and F. Weigend, J. Chem. Theory Comput. **15**, 1028 (2019).
[136]Y. J. Franzke, "Calculation of NMR parameters in a modern relativistic density functional framework: Theory, implementation, and application," Ph.D. dissertation (Karlsruhe Institute of Technology (KIT), Karlsruhe, Germany, 2021).
[137]Y. J. Franzke, F. Mack, and F. Weigend, J. Chem. Theory Comput. **17**, 3974 (2021).
[138]Y. J. Franzke, J. Chem. Theory Comput. **19**, 2010 (2023).
[139]Y. J. Franzke and C. Holzer, J. Chem. Phys. **159**, 184102 (2023).
[140]Y. J. Franzke, "NMR spectroscopic parameters in local exact two-component theory," in *NMR Spectroscopic Parameters: Theories and Models, Computational Codes and Calculations*, edited by G. A. Aucar (Royal Society of Chemistry, Cambridge, United Kingdom, 2025), Chap. 3, pp. 98–134.
[141]Y. J. Franzke, C. Holzer, and F. Mack, J. Chem. Theory Comput. **18**, 1030 (2022).
[142]Y. J. Franzke and C. Holzer, J. Chem. Theory Comput. **22**, 9608 (2026).
[143]C. J. Schattenberg and M. Kaupp, J. Phys. Chem. A **125**, 2697 (2021).
[144]C. J. Schattenberg and M. Kaupp, J. Phys. Chem. A **128**, 2253 (2024).
[145]S. Gillhuber, Y. J. Franzke, and F. Weigend, J. Phys. Chem. A **125**, 9707 (2021).
[146]Y. J. Franzke, F. Bruder, S. Gillhuber, C. Holzer, and F. Weigend, J. Phys. Chem. A **128**, 670 (2024).
[147]D. X. Ngo, K. R. McClain, J. Hrubý, Y. J. Franzke, K. Kundu, H. Kwon, C. A. Gould, B. G. Harvey, S. Hill, and J. R. Long, J. Am. Chem. Soc. **147**, 13799 (2025).
[148]I. Mayer, J. Comput. Chem. **28**, 204 (2007).
[149]M. Kehry, Y. J. Franzke, C. Holzer, and W. Klopper, Mol. Phys. **118**, e1755064 (2020).
[150]M. Olejniczak, R. Bast, T. Saue, and M. Pecul, J. Chem. Phys. **136**, 014108 (2012).
[151]J. Autschbach, Mol. Phys. **111**, 2544 (2013).
[152]S. Komorovský, M. Repiský, O. L. Malkina, and V. G. Malkin, J. Chem. Phys. **132**, 154101 (2010).
[153]M. Repiský, S. Komorovský, O. L. Malkina, and V. G. Malkin, Chem. Phys. **356**, 236 (2009).
[154]F. Krätschmer, X. Sun, S. Gillhuber, H. Kucher, Y. J. Franzke, F. Weigend, and P. W. Roesky, Chem. Eur. J. **29**, e202203583 (2023).
[155]N. Spang, K. Beuthert, T. Z. Kirsch, L. Guggolz, Y. J. Franzke, and S. Dehnen, chemRxiv:10.26434/chemrxiv.15000965/v1 (2026).
[156]H. Günther, F. Weigend, X. Xie, W. Cao, X.-F. Gao, X.-B. Wang, and F. Tambornino, Angew. Chem., Int. Ed. **64**, e202507543 (2025).
[157]K. Dollberg, C. Jakobi, H. Schmücker, R.-M. Richter, F. Weigend, and C. von Hänisch, Organometallics **43**, 2812 (2024).
[158]P. Pracht, S. Grimme, C. Bannwarth, F. Bohle, S. Ehlert, G. Feldmann, J. Gorges, M. Müller, T. Neudecker, C. Plett, S. Spicher, P. Steinbach, P. A. Wesołowski, and F. Zeller, J. Chem. Phys. **160**, 114110 (2024).
[159]S. Gohr, P. Hrobárik, M. Repiský, S. Komorovský, K. Ruud, and M. Kaupp, J. Phys. Chem. A **119**, 12892 (2015).
[160]Y. J. Franzke and J. M. Yu, J. Chem. Theory Comput. **18**, 323 (2022).
[161]Y. J. Franzke and J. M. Yu, J. Chem. Theory Comput. **18**, 2246 (2022).
[162]P. A. B. Haase, M. Repisky, S. Komorovsky, J. Bendix, and S. P. A. Sauer, Chem. Eur. J. **24**, 5124 (2018).
[163]M. Filatov, W. Zou, and D. Cremer, J. Chem. Phys. **139**, 014106 (2013).
[164]F. Bruder, F. Weigend, and Y. J. Franzke, J. Phys. Chem. A **128**, 7298 (2024).
[165]A. Wodyński and M. Kaupp, J. Chem. Theory Comput. **16**, 314 (2020).
[166]C. Holzer and Y. J. Franzke, J. Chem. Phys. **157**, 034108 (2022).
[167]G. Scalmani and M. J. Frisch, J. Chem. Theory Comput. **8**, 2193 (2012).
[168]S. Komorovsky, P. J. Cherry, and M. Repisky, J. Chem. Phys. **151**, 184111 (2019).
[169]Y. J. Franzke, W. M. Schosser, and F. Pauly, Phys. Rev. B **109**, 165144 (2024).
[170]K. Kundu, J. R. K. White, S. A. Moehring, J. M. Yu, J. W. Ziller, F. Furche, W. J. Evans, and S. Hill, Nat. Chem. **14**, 392 (2022).
[171]M. Shiddiq, D. Komijani, Y. Duan, A. Gaita-Ariño, E. Coronado, and S. Hill, Nature **531**, 348 (2016).
[172]J. R. Morton and K. F. Preston, J. Magn. Reson. **30**, 577 (1978).
[173]A. Rajabi, D. K. Nguyen, R. Grotjahn, and F. Furche, Inorg. Chem. **64**, 9477 (2025).
[174]S. Sinnecker and F. Neese, J. Phys. Chem. A **110**, 12267 (2006).
[175]S. Schmitt, P. Jost, and C. van Wüllen, J. Chem. Phys. **134**, 194113 (2011).
[176]F. Neese, in *Calculation of NMR and EPR Parameters: Theory and Applications*, edited by M. Kaupp, M. Bühl, and V. G. Malkin (Wiley VCH, Weinheim, Germany, 2004), Chap. 34, pp. 541–564.
[177]M. Wu, H. Li, W. Chen, D. Wang, Y. He, L. Xu, S. Ye, and G. Tan, Chem **9**, 2573 (2023).
[178]Y. Pang, N. Nöthling, M. Leutzsch, L. Kang, E. Bill, M. van Gastel, E. Reijerse, R. Goddard, L. Wagner, D. SantaLucia, S. DeBeer, F. Neese, and J. Cornella, Science **380**, 1043 (2023).
[179]T. Al Said, D. Spinnato, K. Holldack, F. Neese, J. Cornella, and A. Schnegg, J. Am. Chem. Soc. **147**, 84 (2025).
[180]Y. Schulte, T. Freese, C. Wölper, J. Schulte, G. Haberhauer, and S. Schulz, Angew. Chem., Int. Ed. **64**, e202508250 (2025).
[181]A. Soncini and W. Van den Heuvel, J. Chem. Phys. **138**, 021103 (2013).
[182]B. Martin and J. Autschbach, J. Chem. Phys. **142**, 054108 (2015).
[183]B. Martin and J. Autschbach, Phys. Chem. Chem. Phys. **18**, 21051 (2016).
[184]B. Pritchard, B. Martin, and J. Autschbach, PNMRShift Program, see https://github.com/jautschbach/pnmr-shift/tree/master, 2022 (retrieved 5 May 2026).
[185]See output and manual of the mpshift module for convention of row/columns of tensors for the interface and comparison to other EPR programs.
[186]C. E. Laplaza, M. J. A. Johnson, J. C. Peters, A. L. Odom, E. Kim, C. C. Cummins, G. N. George, and I. J. Pickering, J. Am. Chem. Soc. **118**, 8623 (1996).
[187]A. Pausch and W. Klopper, Mol. Phys. **118**, e1736675 (2020).
[188]S. Blaschke, S. Stopkowicz, and A. Pausch, J. Chem. Phys. **161**, 024117 (2024).
[189]A. Pausch, B. Menges, and Y. J. Franzke, "SAP-X2C in finite magnetic fields" (unpublished) (2026).
[190]A. Pausch, C. Holzer, and W. Klopper, J. Chem. Theory Comput. **18**, 3747 (2022).

12 November 2026 10:29:21

© Author(s) 2026

[191] A. I. Pausch,"Development and application of efficient computational methods for molecular spectroscopy in finite magnetic fields," Ph.D. dissertation (Karlsruhe Institute of Technology (KIT), Karlsruhe, Germany, 2022).
[192] C. Holzer, A. M. Teale, F. Hampe, S. Stopkowicz, T. Helgaker, and W. Klopper, J. Chem. Phys. **150**, 214112 (2019).
[193] C. Holzer, A. Pausch, and W. Klopper, Front. Chem. **9**, 746162 (2021).
[194] C. Holzer, J. Chem. Theory Comput. **19**, 3131 (2023).
[195] K. K. Lange, E. I. Tellgren, M. R. Hoffmann, and T. Helgaker, Science **337**, 327 (2012).
[196] E. I. Tellgren and H. Fliegl, J. Chem. Phys. **139**, 164118 (2013).
[197] M. L. Kronenberger, D. Steinmetz, A. Appenzeller, and A. Pausch, J. Chem. Phys. **163**, 224114 (2025).
[198] D. Steinmetz and A. Pausch, J. Chem. Phys. **162**, 154109 (2025).
[199] M. Kühn and F. Weigend, J. Chem. Theory Comput. **9**, 5341 (2013).
[200] M. Kühn and F. Weigend, J. Chem. Phys. **141**, 224302 (2014).
[201] M. Kühn and F. Weigend, J. Chem. Phys. **142**, 034116 (2015).
[202] P. Norman, D. M. Bishop, H. J. A. Jensen, and J. Oddershede, J. Chem. Phys. **123**, 194103 (2005).
[203] L. S. Cederbaum, W. Domcke, and J. Schirmer, Phys. Rev. A **22**, 206 (1980).
[204] M. Kehry, W. Klopper, and C. Holzer, J. Chem. Phys. **159**, 044116 (2023).
[205] C. Müller, M. Sharma, and M. Sierka, J. Comput. Chem. **41**, 2573 (2020).
[206] W. Li, A. Saleh, M. Sharma, C. Hünecke, M. Sierka, M. Neuhaus, L. Hedewig, B. Bergues, M. Alharbi, H. ALQahtani, A. M. Azzeer, S. Gräfe, M. F. Kling, A. F. Alharbi, and Z. Wang, Adv. Opt. Mater. **11**, 2203070 (2023).
[207] N. Rauwolf, W. Klopper, and C. Holzer, J. Chem. Phys. **160**, 061101 (2024).
[208] C. Holzer and Y. J. Franzke, J. Phys. Chem. Lett. **16**, 3980 (2025).
[209] P. Himmelsbach and C. Holzer, J. Chem. Phys. **161**, 244105 (2024).
[210] P. C. Waterman, Proc. IEEE **53**, 805 (1965).
[211] I. Fernandez-Corbaton, D. Beutel, C. Rockstuhl, A. Pausch, and W. Klopper, ChemPhysChem **21**, 878 (2020).
[212] B. Zerulla, M. Krstić, D. Beutel, C. Holzer, C. Wöll, C. Rockstuhl, and I. Fernandez-Corbaton, Adv. Mater. **34**, 2200350 (2022).
[213] B. Zerulla, C. Li, D. Beutel, S. Oßwald, C. Holzer, J. Bürck, S. Bräse, C. Wöll, I. Fernandez-Corbaton, L. Heinke, C. Rockstuhl, and M. Krstić, Adv. Funct. Mater. **34**, 2301093 (2023).
[214] B. Zerulla, D. Beutel, C. Holzer, I. Fernandez-Corbaton, C. Rockstuhl, and M. Krstić, Adv. Mater. **36**, 2311405 (2024).
[215] B. Zerulla, A. L. Díaz, C. Holzer, C. Rockstuhl, I. Fernandez-Corbaton, and M. Krstić, Adv. Opt. Mater. **12**, 2400150 (2024).
[216] M. Poleva, B. Zerulla, C. Holzer, V. Bonačić-Koutecký, A. Pniakowska, J. Olesiak-Banska, R. Antoine, I. Fernandez-Corbaton, C. Rockstuhl, and M. Krstić, J. Phys. Chem. C **129**, 17119 (2025).
[217] M. Nyman, X. Garcia-Santiago, M. Krstić, L. Materne, I. Fernandez-Corbaton, C. Holzer, P. Scott, M. Wegener, W. Klopper, and C. Rockstuhl, Laser Photonics Rev. **18**, 2300967 (2024).
[218] V. Rai, N. Balzer, G. Derenbach, C. Holzer, M. Mayor, W. Wulfhekel, L. Gerhard, and M. Valášek, Nat. Commun. **14**, 8253 (2023).
[219] B. Zerulla, M. Krstić, S. Chen, Z. Yu, D. Beutel, C. Holzer, M. Nyman, A. Nefedov, Y. Wang, T. G. Mayerhöfer, C. Wöll, and C. Rockstuhl, Phys. Chem. Chem. Phys. **26**, 13683 (2024).
[220] L. Freter, B. Zerulla, M. Krstić, C. Holzer, C. Rockstuhl, and I. Fernandez-Corbaton, Phys. Rev. A **110**, 043516 (2024).
[221] M. Poleva, E. Holzinger, M. Krstić, C. Holzer, I. Fernandez-Corbaton, and C. Rockstuhl, Opt. Mater. Express **16**, 588 (2026).
[222] O. Christiansen, H. Koch, and P. Jørgensen, J. Chem. Phys. **103**, 7429 (1995).
[223] H. Koch, O. Christiansen, P. Jørgensen, A. M. Sanchez de Merás, and T. Helgaker, J. Chem. Phys. **106**, 1808 (1997).
[224] P.-F. Loos, M. Boggio-Pasqua, A. Blondel, F. Lipparini, and D. Jacquemin, J. Chem. Theory Comput. **21**, 8010 (2025).
[225] R. Send, V. R. I. Kaila, and D. Sundholm, J. Chem. Phys. **134**, 214114 (2011).
[226] N. Sülzner and C. Hättig, J. Chem. Theory Comput. **20**, 2462 (2024).
[227] A. Klamt and G. Schüürmann, J. Chem. Soc., Perkin Trans. 2 **22**, 799 (1993).
[228] A. Klamt, J. Phys. Chem. **100**, 3349 (1996).
[229] M. Garcia-Ratés and F. Neese, J. Comput. Chem. **41**, 922 (2020).
[230] M. Scheurer, A. Dreuw, E. Epifanovsky, M. Head-Gordon, and T. Stauch, J. Chem. Theory Comput. **17**, 583 (2021).
[231] F. Zeller, E. Berquist, E. Epifanovsky, and T. Neudecker, J. Chem. Phys. **157**, 184802 (2022).
[232] A. Pausch, F. Zeller, and T. Neudecker, J. Chem. Theory Comput. **21**, 747 (2025).
[233] A. Pausch, J. Phys. Chem. Lett. **17**, 1108 (2026).
[234] M. Okamoto, S. Hirayama, and R. P. Steer, Can. J. Chem. **85**, 432 (2007).
[235] T. Yanai, D. P. Tew, and N. C. Handy, Chem. Phys. Lett. **393**, 51 (2004).
[236] M. Bursch, E. Caldeweyher, A. Hansen, H. Neugebauer, S. Ehlert, and S. Grimme, Acc. Chem. Res. **52**, 258 (2019).
[237] D. Rappoport and F. Furche, J. Chem. Phys. **133**, 134105 (2010).
[238] C. Hättig and A. Pausch, J. Phys. Chem. A **129**, 6155 (2025).
[239] R. Crespo-Otero and M. Barbatti, Theor. Chem. Acc. **131**, 1237 (2012).
[240] E. W. Driscoll, J. R. Hunt, and J. M. Dawlaty, J. Phys. Chem. Lett. **7**, 2093 (2016).
[241] A. Rohatgi, WebPlotDigitizer, Version 5.2, https://automeris.io (retrieved 9 April 2026).
[242] M. Sharma and M. Sierka, J. Chem. Theory Comput. **18**, 6892 (2022).
[243] M. Sharma, "Density functional theory based embedding for molecular and periodic systems," Ph.D. dissertation (Friedrich-Schiller-Universität Jena, Jena, Germany, 2024).
[244] M. Sharma and M. Sierka, J. Chem. Theory Comput. **20**, 9592 (2024).
[245] M. Sharma and D. Mishra, J. Appl. Crystallogr. **52**, 1449 (2019).
[246] F. Weigend, Phys. Chem. Chem. Phys. **8**, 1057 (2006).
[247] L. H. Thomas, Math. Proc. Cambridge Philos. Soc. **23**, 542 (1927).
[248] E. Fermi, Rend. Accad. Naz. Lincei **6**, 602 (1927).
[249] A. Peruzzo, J. McClean, P. Shadbolt, M.-H. Yung, X.-Q. Zhou, P. J. Love, A. Aspuru-Guzik, and J. L. O'Brien, Nat. Commun. **5**, 4213 (2014).
[250] J. Tilly, H. Chen, S. Cao, D. Picozzi, K. Setia, Y. Li, E. Grant, L. Wossnig, I. Rungger, G. H. Booth, and J. Tennyson, "The variational quantum eigensolver: A review of methods and best practices," Phys. Rep. **986**, 1 (2022).
[251] J. Preskill, Quantum **2**, 79 (2018).
[252] W. J. Huggins, J. R. McClean, N. C. Rubin, Z. Jiang, N. Wiebe, K. B. Whaley, and R. Babbush, npj Quantum Inf. **7**, 23 (2021).
[253] J. M. Clary, E. B. Jones, D. Vigil-Fowler, C. Chang, and P. Graf, Int. J. Quantum Chem. **123**, e27097 (2023).
[254] W. Sennane, J.-P. Piquemal, and M. J. Rančić, Phys. Rev. A **107**, 012416 (2023).
[255] I. T. Khan, M. Tudorovskaya, J. J. M. Kirsopp, D. Muñoz Ramo, P. Warrier, D. K. Papanastasiou, and R. Singh, J. Chem. Phys. **158**, 214114 (2023).
[256] L. Zhao, J. Goings, K. Shin, W. Kyoung, J. I. Fuks, J.-K. Kevin Rhee, Y. M. Rhee, K. Wright, J. Nguyen, J. Kim, and S. Johri, npj Quantum Inf. **9**, 60 (2023).
[257] K. Yamamoto, D. Z. Manrique, I. T. Khan, H. Sawada, and D. M. Ramo, Phys. Rev. Res. **4**, 033110 (2022).
[258] N. Yoshioka, T. Sato, Y. O. Nakagawa, Y.-Y. Ohnishi, and W. Mizukami, Phys. Rev. Res. **4**, 013052 (2022).
[259] M. Rossmannek, F. Pavošević, A. Rubio, and I. Tavernelli, J. Phys. Chem. Lett. **14**, 3491 (2023).
[260] A. Ralli, M. Williams de la Bastida, and P. V. Coveney, Phys. Rev. A **109**, 022418 (2024).
[261] L. Mineh and A. Montanaro, Phys. Rev. B **105**, 125117 (2022).
[262] C. Cao, J. Sun, X. Yuan, H.-S. Hu, H. Q. Pham, and D. Lv, npj Comput. Mater. **9**, 78 (2023).
[263] W. Li, Z. Huang, C. Cao, Y. Huang, Z. Shuai, X. Sun, J. Sun, X. Yuan, and D. Lv, Chem. Sci. **13**, 8953 (2022).
[264] A. Javadi-Abhari, M. Treinish, K. Krsulich, C. J. Wood, J. Lishman, J. Gacon, S. Martiel, P. D. Nation, L. S. Bishop, A. W. Cross, B. R. Johnson, and J. M. Gambetta, "Quantum computing with Qiskit," arXiv:2405.08810 (2024).
[265] V. Bergholm, J. Izaac, M. Schuld, C. Gogolin, S. Ahmed, V. Ajith, M. S. Alam, G. Alonso-Linaje, B. AkashNarayanan, A. Asadi, J. M. Arrazola, U. Azad, S.

12 November 2026 10:29:21

© Author(s) 2026

Banning, C. Blank, T. R. Bromley, B. A. Cordier, J. Ceroni, A. Delgado, O. D. Matteo, A. Dusko, T. Garg, D. Guala, A. Hayes, R. Hill, A. Ijaz, T. Isacsson, D. Ittah, S. Jahangiri, P. Jain, E. Jiang, A. Khandelwal, K. Kottmann, R. A. Lang, C. Lee, T. Loke, A. Lowe, K. McKiernan, J. J. Meyer, J. A. Montañez-Barrera, R. Moyard, Z. Niu, L. J. O'Riordan, S. Oud, A. Panigrahi, C.-Y. Park, D. Polatajko, N. Quesada, C. Roberts, N. Sá, I. Schoch, B. Shi, S. Shu, S. Sim, A. Singh, I. Strandberg, J. Soni, A. Száva, S. Thabet, R. A. Vargas-Hernández, T. Vincent, N. Vitucci, M. Weber, D. Wierichs, R. Wiersema, M. Willmann, V. Wong, S. Zhang, and N. Killoran, "PennyLane: Automatic differentiation of hybrid quantum-classical computations," arXiv:1811.04968 (2022).

[266]M. Sharma, Webpage of RIPER-Tools, https://ripertools.turbomole.org (retrieved 10 June 2026).

[267]S. Grimme, S. Ehrlich, and L. Goerigk, J. Comput. Chem. **32**, 1456 (2011).

[268]D. Vilela Oliveira, J. Laun, M. F. Peintinger, and T. Bredow, J. Comput. Chem. **40**, 2364 (2019).

[269]A. Lembarki and H. Chermette, Phys. Rev. A **50**, 5328 (1994).

[270]K. Hui and J.-D. Chai, J. Chem. Phys. **144**, 044114 (2016).

[271]See https://www.turbomole.org for TURBOMOLE website (retrieved 22 March 2026).

12 November 2026 10:29:21

© Author(s) 2026